Precipitation and Cloud Structure in Midlatitude Cyclones

PAUL R. FIELD

National Center for Atmospheric Research, Boulder, Colorado

ROBERT WOOD

University of Washington, Seattle, Washington

(Manuscript received 14 February 2006, in final form 3 May 2006)

ABSTRACT

Composite mean fields and probability distribution functions (PDFs) of rain rate, cloud type and cover, cloud-top temperature, surface wind velocity, and water vapor path (WVP) are constructed using satellite observations of midlatitude cyclones from four oceanic regions (i.e., the North Pacific, South Pacific, North Atlantic, and South Atlantic). Reanalysis surface pressure fields are used to ascertain the locations of the cyclone centers, onto which the satellite fields are interpolated to give a database of ~1500 cyclones from a two-year period (2003–04). Cyclones are categorized by their strength, defined here using surface wind speed, and by their WVP, and it is found that these two measures can explain a considerable amount of the intercyclone variability of other key variables. Composite cyclones from each of the four ocean basins exhibit similar spatial structure for a given strength and WVP. A set of nine composites is constructed from the database using three strength and three WVP ranges and is used to demonstrate that the mean column relative humidity of these systems varies only slightly (0.58–0.62) for a doubling in WVP (or equivalently a 7-K rise in sea surface temperature) and a 50% increase in cyclone strength. However, cyclone-mean rain rate increases markedly with both cyclone strength and WVP, behavior that is explained with a simple warm conveyor belt model. Systemwide high cloud fraction (tops above 440 hPa) increases from 0.23 to 0.31 as cyclone strength increases by 50%, but does not vary systematically with WVP. It is suggested that the composite fields constitute useful diagnostics for evaluating the behavior of large-scale numerical models, and may provide insight into how precipitation and clouds in midlatitude cyclones respond under a changed climate.

1. Introduction

Midlatitude, or extratropical, cyclones (hereafter referred to simply as cyclones) are an important component of the atmospheric general circulation due to their ability to redistribute large amounts of heat, moisture, and momentum (e.g., Hartmann 1994). Cyclones are driven by temperature gradients between the warm subtropics and the cold polar regions and are the primary atmospheric conduit for poleward energy transfer in the midlatitudes (Oort 1971; Trenberth and Stepaniak 2003). Their influence on weather and climate and their consequences for life have resulted in extensive study of these systems, and a rich literature concerning the synoptic nature of cyclones extends from the Norwegian conceptual model introduced by Bjerknes (1919) through to the recent reviews edited by Newton and Holopainen (1990) and Shapiro and Grønas (1999).

Most conceptual models and numerical model investigations of cyclones focus primarily on their dynamical structure and their interaction with the midlatitude jet. There also exists an extensive literature concerning the classification of cyclones based on satellite imagery (e.g., Evans et al. 1994 and references within) that seeks to relate the observed cloud structures to dynamical features and aid in the understanding of cyclogenesis. Satellite imagery, weather radar, and surface observations have all been invaluable tools for the analysis of the mesoscale structure of cloud, precipitation, and winds within cyclones, but this analysis has been largely limited to case studies (e.g., Harrold 1973; Neiman et al. 1993; Browning and Roberts 1996; Stoelinga et al. 2003; Browning 2004). Such case studies have contributed heavily to the generation of conceptual

Corresponding author address: Paul Field, NCAR, 3450 Mitchell Lane, Boulder, CO 80301.
E-mail: prfield@ucar.edu

DOI: 10.1175/JCLI3998.1

models of cyclones that provide a framework for understanding the internal dynamical evolution of cyclones.

Recent studies are using reanalysis datasets to study the structure and evolution of cyclones (e.g., Hoskins and Hodges 2005). Reanalysis uses data assimilation techniques to combine disparate observations of the atmospheric structure into a framework consistent with general circulation model physics. Through recent developments in data assimilation (Kalnay 2003), reanalysis datasets have improved to the point where they now provide credible thermodynamic and dynamic fields. Unfortunately, the assimilation of precipitation and cloud data is in its infancy (e.g., Hou et al. 2001; Janiskova et al. 2002). Taken together with the fact that clouds and precipitation are sensitive to small changes in moisture and temperature, and are strongly influenced by processes occurring on scales smaller than a typical global model grid box, the result is that clouds and precipitation in reanalysis datasets are strongly dependent upon the particular parameterization in the underlying model. As a result, significant deficiencies are apparent when compared with cloud observations (Chevalier et al. 2001). We have chosen to use satellite retrievals of precipitation data rather than reanalysis datasets to avoid any biases introduced by microphysical schemes, but note that biases may exist within the satellite datasets that are introduced by the retrieval algorithm used. Several of these datasets offer near-global daily coverage of important cloud and precipitation parameters and we will use these data in conjunction with reanalysis dynamic and thermodynamic data in this study.

Perhaps the first quantitative compositing of cyclones was carried out by Petterssen et al. (1962) using 51 cases, from which cyclone-relative maps of predominant weather types and heat fluxes were produced. More recent compositing of approximately 200 cyclones (Lau and Crane 1995), by averaging the cyclone structure at a point (or collection of points) on the earth's surface relative to the passage of the peak in observed cloud optical thickness, resulted in cyclone composites relative to the thickest cloud rather than relative to the low pressure center. This methodology for compositing cyclone data, the first involving quantitative cloud data, clearly delineates the variability in cloud structure across the composite cyclone system, with a shield of high-top thick cloud extending toward the east of the low center and medium-top and low-top cloud over the center and to the west of the surface low center. This methodology was also used to evaluate the European Centre for Medium-Range Weather Forecasts (ECMWF) model-derived clouds (Lau and Crane 1997; Klein and Jakob 1999). Cyclone center-relative compositing has also been used to examine the rapid intensification of midlatitude cyclones (Wang and Rogers 2001), the extratropical transition of tropical storms (Sinclair 2002), and non-cyclone-centric compositing methodologies have been used to distinguish different large-scale flow regimes within midlatitudes (e.g., Tselioudis et al. 2000; Eckhardt et al. 2004). More recently, Norris and Iacobellis (2005) composited cloud observations at midlatitudes in the North Pacific relative to the maximum warm and cold SST advections and examined the composites by segregating the data into different SST advection and lower-tropospheric static stability regimes. Chang and Song (2006) carried out seasonal compositing of extratropical cyclones, relative to their low pressure centers, from both the North Atlantic and North Pacific. They found that the seasonal composites vary between the two basins and suggest that the differences may be related to variations in static stability, moisture availability, and dynamical forcing.

The ability of compositing to represent the cloud spatial variability in cyclones with a fidelity consistent with the underlying dynamics of the system is encouraging. In this study we use reanalysis data to determine a cyclone-center-relative coordinate system into which various satellite data are transformed and then composited to provide a view of a cyclone from the perspective of the low pressure center. Additionally, by avoiding fixed geographic points as used in Lau and Crane and only using data over oceans we minimize problems associated with land–sea interfaces, such as orography and roughness effects, and uncertainties in satellite retrievals over land.

Application of this work is twofold: First, cyclone-relative compositing provides more generality than individual cyclone case studies, but without losing useful regime-specific system information that is lost in simple spatial averaging (e.g., zonal means). It is also a quantitative framework for critically testing the ability of climate and weather prediction models to produce physically realistic cyclone structure and the moist processes associated with them. Unlike case studies, the composite analysis provides the opportunity to test model variability as well as the mean behavior of each variable against the observed dataset. Second, by compositing cyclones with respect to their strength and water vapor (which is strongly temperature dependent), we hope to provide some insights into the processes that couple the clouds and precipitation to the mesoscale dynamics and thermodynamics of the cyclones.

We have approached this compositing exercise assuming the following two premises: 1) On average a cyclone will exhibit similar precipitation and cloud

structure to another cyclone if the thermodynamic and mesoscale dynamical environments are comparable and 2) The thermodynamic and mesoscale dynamical environment for each cyclone can be categorized by two metrics that represent the mean atmospheric moisture and the mean cyclone strength. It has been previously surmized that the structural properties of clouds and precipitation within cyclones are a response to both their mesoscale dynamics and thermodynamic environment (e.g., Norris and Iacobellis 2005; Chang and Song 2006). The intention of this study is to show that much of the variation between the precipitation and cloud composites of cyclones, for example, seasonal variability, can be understood quantitatively in terms of cyclone strength and atmospheric moisture. Understanding the change in cyclone cloudiness and precipitation with respect to these two metrics will allow us to quantitatively answer questions posed by studies that suggest mean cyclone strength and frequency are changing as a result of climate change.

The structure of the paper is as follows. In section 2 we describe the data used. A simple precipitation model is outlined in section 3. The compositing technique and methodology is outlined in section 4. Section 5 describes the results for the North Atlantic while section 6 compares the different regions. Conditional sampling based on cyclone strength and atmospheric moisture is examined in section 7. The results are discussed in section 8 and summarized in section 9.

2. Satellite and reanalysis data

a. Cloud data

The cloud data used in this study are derived from level-3 aggregated pixel level data from the Moderate Resolution Imaging Spectroradiometer (MODIS) on the NASA *Terra* sun-synchronous satellite (King et al. 1992). The MODIS cloud product uses visible/near-IR radiances (King et al. 2003) to derive cloud optical depth τ for cloudy pixels in daytime (~1030 LST) scenes. Based upon error analyses (Pincus et al. 1995; King et al. 1997), a conservative error for the pixel level τ estimates is roughly 20%–40%, although the relative error from pixel to pixel is likely to be considerably less than this.

The MODIS cloud mask (Ackerman et al. 1998) is used to determine which pixels are cloudy, and therefore the cloud fractional coverage CF. Cloud top temperature T_{top} is determined using the thermal infrared retrieval described in (Ma et al. 2000). The MODIS level-3 data are averages and histograms derived from the pixel level on a $1^\circ \times 1^\circ$ grid. In this study we use the joint histogram, provided in the level-3 dataset, of τ and T_{top} for each grid box. Separate joint histograms are stored for those pixels determined to be ice and water, respectively, by the MODIS cloud phase algorithm King et al. (1997). Temperature bins are 5 K wide for both water and ice cloud $\tau - T_{\text{top}}$ histograms. There are 12 bins for water from 230 to 290 K, and 10 for ice from 220 to 270 K. Optical depth bins, which are quasi-logarithmically spaced, are centered on $\tau = 1, 3, 5, 7, 9, 12.5, 17.5, 25, 35, 45$, and 75 for water clouds and $\tau = 0.25, 0.75, 1.75, 3.75, 6.25, 8.75, 12.5, 17.5, 25, 40$, and 75 for ice clouds.

b. AMSR-E

The Advanced Microwave Scanning Radiometer (AMSR-E), on the NASA *Aqua* sun-synchronous satellite, provides nearly complete coverage each day of several important parameters used in this study. We use AMSR-E data (version 5) provided by Remote Sensing Systems (RSS). For this study we use surface rain rate and column-integrated water vapor estimates [i.e., water vapor path (WVP); Wentz 1997; Wentz and Spencer 1998) and sea surface temperature (SST) estimates Wentz and Meissner (2000). Additional information regarding these products is available online at www.remss.com.] The estimates are made using brightness temperatures observed at four frequencies (10.7, 18.7, 23.8, 36.5, and 89 GHz) and are available only over ocean. The data are provided at a resolution of $0.25^\circ \times 0.25^\circ$ grid and averaged up to the common $1^\circ \times 1^\circ$ grid for analysis. Daily mean fields of each parameter are constructed from an average of data from both daytime (~1330 LST) and nighttime (~0130 LST) overpasses. The WVP product is estimated to have a random error of 1.2 kg m^{-2} and has no bias with respect to rain rate as ascertained through comparison with radiosonde ascents (Wentz 1997) supporting the assertion made by Wentz and Spencer that their algorithm results in minimal cross talk between the retrieved parameters (i.e., rain rate, water vapor).

Uncertainty in the rain rate estimate is more difficult and a complete error characterization does not yet exist (Kummerow et al. 2006). However, we note that the Tropical Rainfall Measuring Mission (TRMM) emittance-based rain rate retrieval (3A11) is very similar to the TRMM Bayesian model approach retrieval (3A12) (see Kummerow et al. 2006; Berg et al. 2006). The Bayesian approach is expected to have an instantaneous rain rate uncertainty of 60% (L'Ecuyer and Stephens (2002). Kummerow et al. (2006) also show that a simple emmittance retrieval method has an instantaneous uncertainty of a factor of 2 based on uncertainties in the brightness temperature measurements. Based on these results we will assume that the

instantaneous uncertainty in the Wentz and Spencer (1998) algorithm is also ~60%, which is reduced to about 20% after averaging up to a 100-km grid box. One shortcoming of the rain rate data used here is that they will probably have a lowered success rate in detecting isolated convective activity often present in the cold sector of cyclones. Seasonal mean comparisons between the TRMM precipitation radar rain rate and the emittance-based rain rate indicate that the latter method may underestimate midlatitude rain rate by about 20% because of this problem (Berg et al. 2006). However, that estimate assumes that the precipitation radar is unbiased, which is currently not known. Additionally, TRMM samples mostly outside of our analysis areas, which makes it difficult to make concrete inferences about biases in the most baroclinically unstable regions. In the following analysis we will assume that the bias in the rain rate used is zero, but we will return to this in more detail in the discussion.

c. QuikSCAT

Surface wind vector data are from the SeaWinds 13.4-GHz microwave scatterometer on the NASA Quikbird sun-synchronous platform. The local overpass times for Quikbird are ~0600 and 1800 LST, and we average both passes to provide a daily field. The SeaWinds instrument measures backscatter from wind-driven capillary waves at a number of viewing angles allowing estimates to be made of wind speed and direction with approximately 25-km horizontal resolution. In this study we use the products generated by RSS using the algorithm of Wentz and Smith (1999). The swath width guarantees almost complete daily coverage in the regions studied. The data are provided at a resolution of $0.25° \times 0.25°$ grid and averaged up to the common $1° \times 1°$ grid for analysis.

Four satellite microwave radiometers on the SSM/I and TRMM platforms are used to determine and reject QuikSCAT data where significant rain is present, as the rain's impact on surface capillary waves precludes accurate wind retrievals. Contreras et al. (2003) show that, if rain completely fills the scatterometer footprint, then no retrieval can be made if the wind speed is below 10 m s^{-1}. In general, only about 7% of the QuikSCAT data are rain contaminated over the regions used in this study. Nevertheless, we accept that this is a potential source of bias in our analyses. An examination of cyclone-relative composite maps showing the fraction of missing data does not show a strong loss of coverage due to rain even in the sectors of the cyclone with high mean rain rate, so we consider its potential impact to be relatively small.

Through comparison with 10-m wind measurements from buoys, Chelton and Freilich (2005) determined that the random error present in the 25-km resolution QuikSCAT winds is 1.7 m s^{-1}. This error is much reduced for wind speeds between 6 and 15 m s^{-1} . There is also a directional error of 14° for wind speeds in excess of 6 m s^{-1}, which increases for slower wind speeds . These random errors will be reduced by a factor of 4 when averaged over a 100-km grid box.

d. Reanalysis datasets

Reanalysis surface pressure (p_0) fields from National Center for Environmental Prediction–National Center for Atmospheric Research (NCEP–NCAR; Kistler et al. 2001) are used to determine the cyclone center locations. We use daily reanalysis data on a $2.5° \times 2.5°$ grid that is interpolated onto the same $1° \times 1°$ grid as the satellite data prior to analysis. We use temperature profiles from the reanalysis (obtained at 1000, 925, 850, 700, 600, 500, 400, and 300 hPa) to (i) enable conversion of MODIS temperature optical depth histograms to pressure–optical depth histograms, and (ii) to estimate the saturated water vapor path for each column as described in section 2e.

e. Derived datasets

We derive a column relative humidity $\mathrm{RH_{col}}$ using the method of Bretherton et al. (2004). Reanalysis temperature profiles are used to estimate the water vapor path for a completely saturated column $\mathrm{WVP_{sat}} = \int[q_{\mathrm{sat}}(T, p)/g]\, dp$, where q_{sat} is the saturation water vapor mixing ratio and g is the gravitational acceleration. We then define $\mathrm{RH_{col}}$ as the ratio of observed to saturated water vapor path: that is,

$$\mathrm{RH_{col}} = \mathrm{WVP}/\mathrm{WVP_{sat}}$$

We use a cloud-type classification similar to that defined in the International Satellite Cloud Climatology Project (ISCCP) in which nine cloud types are defined based upon cloud top pressure p_{top} and optical depth τ (Rossow and Schiffer 1991). The derived $\tau - p_{\mathrm{top}}$ joint histograms (obtained by combining MODIS $\tau - T_{\mathrm{top}}$ histograms with reanalysis temperature profiles) are used to generate composite fields of cloud coverage by each of the cloud types. We have renamed the "deep convective" type to "deep frontal" as we feel that this is a more appropriate definition for the optically thick high clouds in midlatitude cyclones. The pressure categories used were $p_{\mathrm{top}} < 440$ hPa, $440 < p_{\mathrm{top}} < 710$ hPa, $p_{\mathrm{top}} > 710$ hPa for high-, mid-, and low-level cloud, respectively. Cloud optical depth thresholds used to classify clouds into optically thin, medium, and thick types are $\tau < 5$, $5 < \tau < 25$, and $\tau > 25$, respectively, for

water clouds, and $\tau < 3.75$, $3.75 < \tau < 25$, and $\tau > 25$, respectively, for ice clouds. These categories are slightly different to those used by ISCCP, but they are as close as is possible given the joint histogram bins used in the MODIS level-3 data.

3. Warm conveyor belt rain rate

We consider a simple precipitation model to compare with the observations. The intention is to not supplant what can be accomplished with detailed microphysical modeling, but to provide a simple framework for understanding the variation of the composited rain rates with respect to cyclone strength and atmospheric moisture.

We can explain the observed changes in the composite mean rain rate using an argument based on a simple analytical warm conveyor belt (WCB) model described by Harrold (1973) and Carlson (1998). It is assumed that all of the moisture transported along and up the WCB is rained out. The rate of water mass loaded onto the WCB is $M_{\rm wcb} = \rho_0 q_0 V_{bl} h_{bl}\, w_{\rm wcb}$, where ρ_0 and q_0 are the air density and water vapor mixing ratio, respectively, in the planetary boundary layer (PBL) where the WCB originates; $V_{\rm bl}$ is the wind speed in the PBL; $h_{\rm bl}$ is the depth of the boundary layer (that contains most of the moisture); and $w_{\rm wcb}$ is the width of the conveyor belt. To convert $M_{\rm wcb}$ to a rain rate we simply divide by the area over which rain falls. The cyclone-mean rain rate from the WCB model is $R_{\rm wcb} = \rho_0 q_0 V_{\rm bl} h_{\rm bl} w_{\rm wcb}/A_c$, where A_c is the cyclone area $[=\pi(2000\ {\rm km})^2]$. Assuming that $V_{\rm bl} = \langle V\rangle$ where the angled brackets represent the mean over a circle of radius 2000 km located at the center of the domain (see next section), and $\rho_0 q_0 = k\,\langle {\rm WVP}\rangle/S$ where S is a water vapor scale height, $h_{\rm bl} = S$, k is a constant that accounts for the fact that the equatorward side of the cyclone is more moist than the mean value, and letting $c = w_{\rm wcb}k/A_c$ gives

$$R_{\rm wcb} = c\langle {\rm WVP}\rangle\langle V\rangle. \tag{1}$$

We note that for this model the controlling variables are within the composite domain, but it may be the case that some of the moist warm air is advected from well outside of the domain and, as a consequence, the implied width of the warm conveyor belt may seem large compared to case study analyses (e.g., Harrold 1973). To some extent this is expected because the warm conveyor belt will be a composite of many cases and so will naturally be broader than in single realizations. While we accept that it is not perfect, we will show that this simple model, controlled by two cyclonewide averaged metrics, can be used to quantitatively predict with some skill the cyclonewide-averaged rain rate.

4. Compositing methodology

To locate the cyclones we use a surface pressure anomaly p_0' derived by removal from the daily p_0 field (smoothed with four passes of a 2° wide boxcar function) of the sliding window monthly mean surface pressure $\langle p_0\rangle$. This eliminates most of the spectral "ringing" in the reanalysis surface pressure field. From the (p_0') field we derive first- and second-order derivatives that are thresholded to obtain candidate grid points to represent the cyclone center:

$$\left(\frac{dp_0'}{dx}\frac{dp_0'}{dy} < 4\times 10^{-5}\ {\rm hPa\ km^{-2}} \quad \text{and} \right.$$

$$\left.\frac{d^2p_0'}{dx^2} + \frac{d^2p_0'}{dy^2} > 9\times 10^{-5}\ {\rm hPa\ km^{-2}}\right).$$

These candidates were then filtered to locate the maximum negative anomaly within a 2000-km radius with a $p_0 < 1015$ hPa. Therefore a single cyclone throughout its evolution could be identified as separate systems on consecutive days. From the global analysis of cyclone locations we focus the analysis in this paper upon four subregions: North Pacific (30°–55°N, 145°E–165°W); North Atlantic (30°–60°N, 10°–50°W); South Pacific (30°–55°S, 120°W–180°); and South Atlantic (30°–55°S, 50°W–10°E). Cyclone centers must be located within these domains to be considered for analysis. Other cyclone location methods, for example, based on vorticity (Sinclair and Watterson 1999) will produce different samples of cyclones. However, our requirement is that we simply sample a wide range of cyclones and we believe that the simple gradient method employed here is sufficient to accomplish that goal.

Figure 1 shows probability distribution functions of the cyclone center surface pressure p_0, pressure anomaly p_0', and a cyclone size defined as the mean radius at which the pressure anomaly decreases to 0.75 of the minimum (most negative) value, which we could argue represents ~⅛ wavelength of the cyclone. Figure 1 indicates that there are no major systematic differences in the depth or size of the cyclones in the four regions. The mode in the pressure anomaly is located at ~14 mb. The cyclone size PDF is positively skewed and has a mode at ~400–500 km from which we can infer a typical cyclone wavelength of 3200–4000 km, which is in agreement with linear baroclinic instability theory where optimum growth is predicted for cyclones of 3500-km wavelength (see Bjerknes and Holmboe 1944). We find that cyclone size is uncorrelated with either latitude or pressure anomaly. In contrast, the size

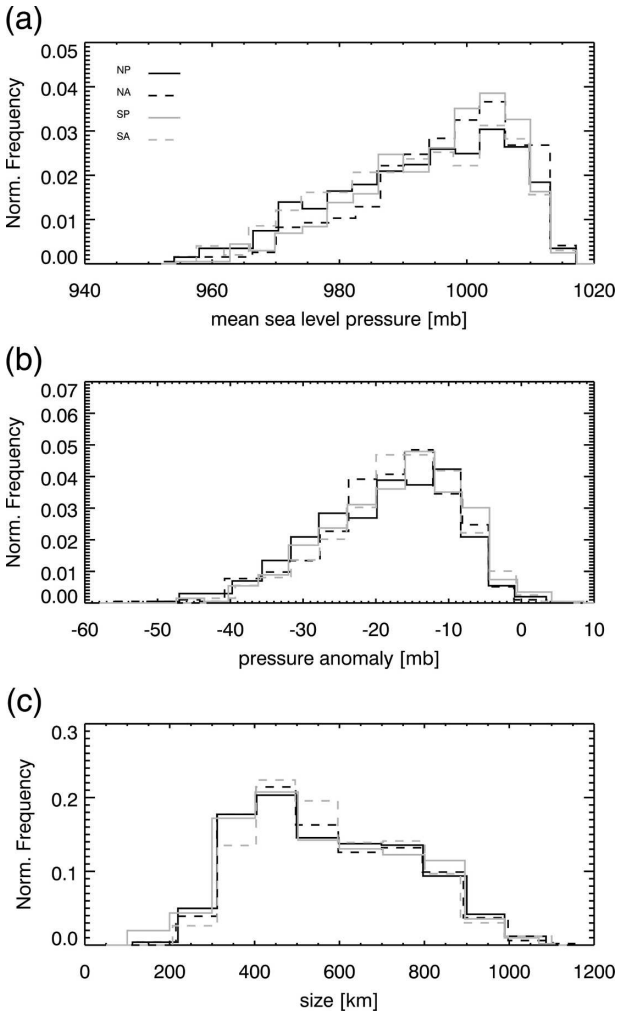

FIG. 1. Frequency distributions for the four regions used in the analysis. NP: North Pacific, NA: North Atlantic, SP: South Pacific, SA: South Atlantic. (a) Mean sea level pressure and (b) pressure anomaly. (c) Cyclone size index defined as the distance from the cyclone center where the pressure anomaly is reduced to 0.75 of the central value.

of the longitudinal extent of cyclones varies by a factor of 2 between 30° and 60° latitude, which suggests that a grid based upon distance, and not latitude–longitude, is most appropriate for compositing cyclones.

For each cyclone the satellite fields (initially all on a $1° \times 1°$ grid) are translated and regridded using bilinear interpolation onto a 4000 by 4000 km^2 domain (x, y are the eastward and northward coordinates, respectively) with 100-km grid spacing and the cyclone located centrally ($x = 0$, $y = 0$). We considered a number of potential rotation and rescaling options according to the location of frontal surfaces and the cyclone size, but decided against using these as rescaling, in particular, would lead to difficulty in the subsequent compositing of the data and it was difficult to objectively locate frontal surfaces using either the satellite or reanalysis data.

After regridding data onto the cyclone-centric domain, statistics are derived from the resulting ensemble of cyclones. Prior to the computation of the mean and PDF, the cyclone database is filtered to remove systems where the fraction of nonmissing SSTs colder than 278 K, as determined from AMSR, exceeds 0.3. This filtering is performed so that potential problems with the rain rate estimates related to near-surface freezing levels are avoided.

First we present composite results from all the North Atlantic cyclones observed during all seasons. Later we examine cyclone properties as a function of cyclone strength and atmospheric moisture metrics that are defined as follows. *Cyclone strength,* $\langle V \rangle$, is determined as the mean surface wind speed, measured using QuikSCAT, within a circle of 2000-km radius centered on the cyclone. Typically, the central pressure anomaly is used to define the cyclone strength. There are two reasons for preferring $\langle V \rangle$ as an indicator of cyclone strength. First, using observed wind speed minimizes our dependence upon reanalyses. Second, the WCB model suggests that $\langle V \rangle$ is a more natural indicator of cyclone strength from a cloud and precipitation perspective.

Our atmospheric *cyclone moisture* metric, ⟨WVP⟩, is similarly defined as the mean AMSR water vapor path within a circle of 2000-km radius centered on the cyclone. We choose a measure of the atmospheric moisture content as an additional metric because of its importance in cloud and precipitation processes. Because the WVP composite fields tend to be symmetric and the north–south gradient is approximately linear, the value of ⟨WVP⟩ is close to the value for WVP found at the center of the cyclone. We find that the symmetry of the composite WVP field means that the effect of stronger cyclones advecting more moist air poleward is countered by the effect of drier air being advected equatorward and, hence, this measure of cyclone moisture is largely independent of cyclone strength over the scale of the domain considered. Additional confirmation of this assertion will be seen later when it is shown that ⟨WVP⟩ is strongly related to ⟨SST⟩, as expected from a water vapor feedback argument, and is unaffected by storm strength.

Seemingly contrary to the above statement is the observation that $\langle V \rangle$ and ⟨WVP⟩ are negatively correlated ($r = -0.6$). This is because of the larger-scale structure of the atmosphere–ocean system that tends to locate stronger storms preferentially toward the polar (and hence drier) edges of the study regions (Fig. 2). This larger-scale correlation does not invalidate the discus-

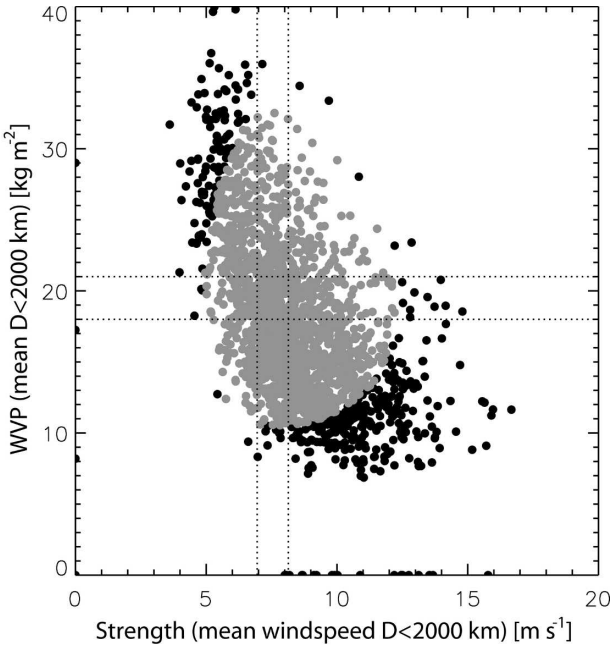

FIG. 2. Scatterplot of cyclone strength (mean wind speed within 2000 km of cyclone center $\langle V \rangle$) and atmospheric moisture (mean water vapor path within 2000 km of cyclone center $\langle \mathrm{WVP} \rangle$). The circles represent all of the cyclones located within the four regions (~1500). The gray circles represent the subset of circles used in the conditional sampling that satisfy the following relation: $[(\log_{10}\langle V \rangle - \overline{\log_{10}\langle V \rangle})/0.2]^2 + [(\log_{10}\langle \mathrm{WVP} \rangle - \overline{\log_{10}\langle \mathrm{WVP} \rangle})/0.25]^2 < 1$, where $\overline{\log_{10}\langle V \rangle} = 0.89$ and $\overline{\log_{10}\langle \mathrm{WVP} \rangle} = 1.27$ are mean values from the whole database. The dotted lines delineate the boundaries of the nine bins used in the conditional sampling. The use of a subset of the cyclones ensures that there is no monotonic variation in the mean variables along each row and column.

sion above concerning storm-scale advection of moisture and our choice of moisture metric. Because of the large-scale correlation exhibited by $\langle V \rangle$ and $\langle \mathrm{WVP} \rangle$, analyses that condition on strength alone may therefore result in an inadvertent and undesirable aliasing of moisture-dependent properties. The use of two metrics to characterize cyclones is possible because of the large database used in this study and allows us to separate thermodynamic (WVP is strongly temperature dependent) and dynamic effects upon cloud and precipitation properties. Later in the analysis we will conditionally sample the cyclones based on the strength and moisture metrics by binning in terms of $\langle V \rangle$ and $\langle \mathrm{WVP} \rangle$. To avoid obtaining monotonically increasing $\langle V \rangle$ for nominally constant $\langle \mathrm{WVP} \rangle$ bins we need to effectively reduce the correlation between these variables. Therefore we have produced a subset of the database that reduces the correlation ($r = -0.4$) and ensures that outliers are excluded from the analysis. The reduced database consists of ~1300 cyclones (from an original database of ~1500).

We find that cyclones in the Southern Hemisphere are similar to their Northern Hemisphere counterparts for similar *cyclone strength* and *atmospheric moisture* (this is justified in section 6). We therefore reflect the Southern Hemisphere cyclones about a zonal axis ($x \rightarrow x, y \rightarrow -y$) and combine all of the cyclones to give a complete database of ~1300 cyclones with a Northern Hemisphere sense. Conditional sampling of the cyclones into three moisture categories ($\langle \mathrm{WVP} \rangle$: 10–18, 18–21, 21–33 kg m^{-2}) and three strength categories ($\langle V \rangle$: 4.9–6.95, 6.95–8.14, 8.14–12.3 m s^{-1}) produces nine composite categories each containing at least 69 members.

5. North Atlantic composite cyclones

a. Mean field

These composite fields are constructed from the ~400 individual cyclones sampled in the North Atlantic. The standard error in the mean value (determined from the sampled distribution at a given grid box in the domain and assuming no bias in the satellite retrievals) is typically 1%–3% for the parameters examined here, except for the rain rates where it is closer to 20%. When viewing the composites it should be borne in mind that the mean field does not necessarily represent what one would observe for a single realization of a cyclone.

1) WIND SPEED

The strongest surface winds are located in an asymmetric ring collocated with the cyclone center. The highest mean wind speeds (12 m s^{-1}) are found 500 km southwest of the center and act to draw cold, dry, polar air around the south of the cyclone (Fig. 3a). The clearly defined "eye" at the center of the cyclone lends credence to the reanalysis cyclone locations and the compositing methodology in general.

2) WATER VAPOR PATH

The contours for this field exhibit a well-defined rotated "S" shape and clearly indicate that a tongue of dry air is wrapped around the western flank of the cyclone and extends to the south of the low center (Fig. 3b), while a warm moist tongue, related to the warm conveyor belt, is seen to the east of the cyclone extending northward.

3) COLUMN RELATIVE HUMIDITY ($\mathrm{RH_{COL}}$)

The mean field of this parameter exhibits a distinct "comma" shape to the east of the cyclone center with a maximum value (>0.75) situated approximately 200 km to the north of the cyclone center (Fig. 3c). High values

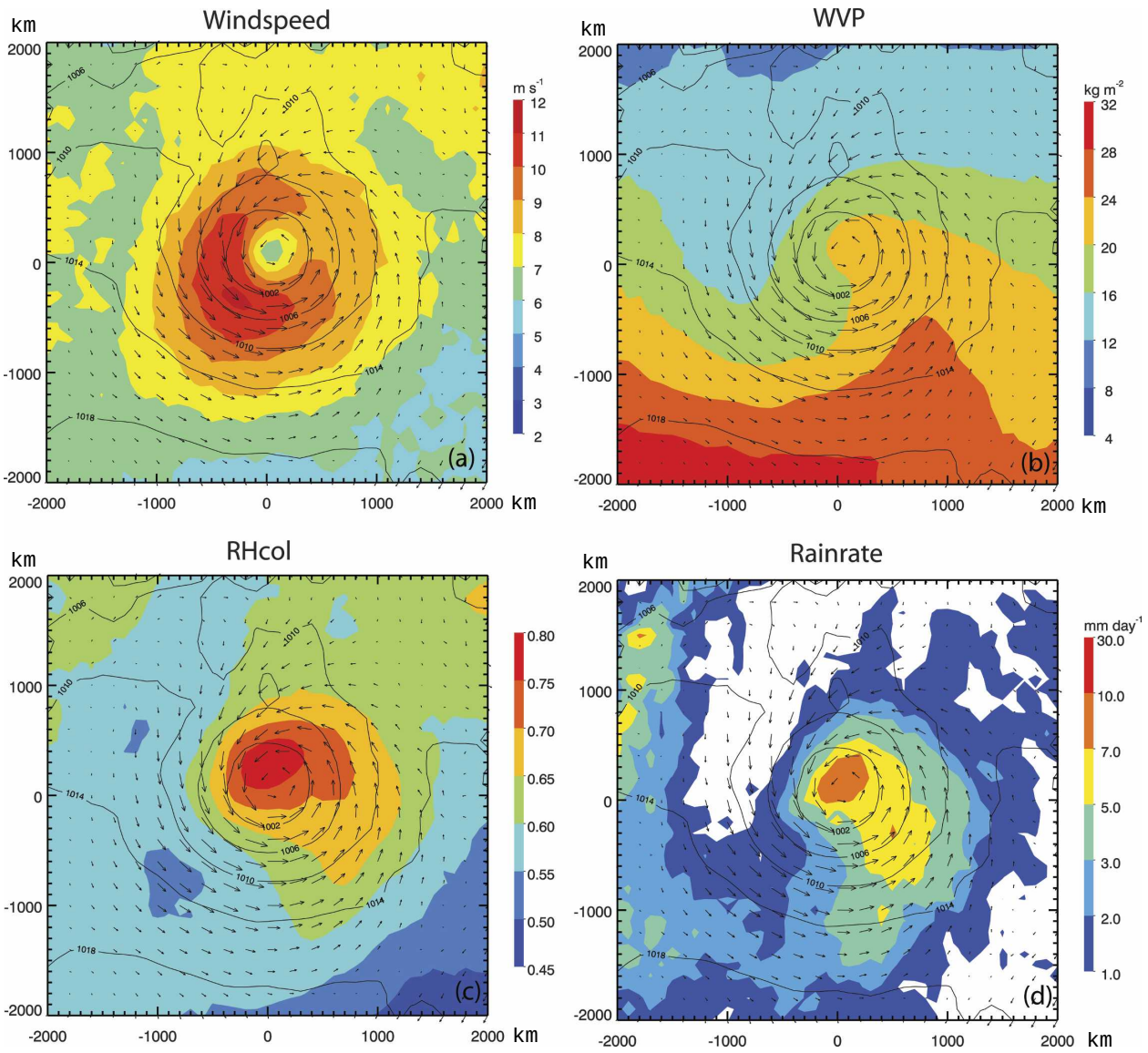

FIG. 3. North Atlantic composite mean fields from ~400 individual cyclones. The mean field mean sea level pressure and QuikSCAT surface wind vectors are overplotted in each diagram. The filled contours represent (a) QuikSCAT surface wind speed, (b) AMSR water vapor path, (c) column relative humidity (see section 2e), and (d) AMSR rain rate.

of RH_{col} are indicative of saturated conditions through a deep layer of the troposphere.

4) RAINFALL RATE

Rain rates of 7–10 mm day^{-1} are found near the center of the cyclone (Fig. 3d) and a curved swath of high rain rates extends to the southeast of the cyclone center before swinging toward the southwest. The relatively high values along the western extreme of the domain represent neighboring systems, which cannot be completely excluded using this compositing method. It can be seen that there is a broad correlation of rain rate with RH_{col} and the moist water vapor tongue representing the warm conveyor belt, confirming that most of the rainfall is associated with this feature, in accordance with other studies (e.g., Harrold 1973; Eckhardt et al. 2004).

5) CLOUD-TOP TEMPERATURE

An arc of cold clouds ($T_{top} < 245$ K) extends from just north of the cyclone center toward the east and southeast, consistent with the expected location of extensive high clouds associated with the warm front (Fig. 4a). In contrast, the southwest quadrant is dominated

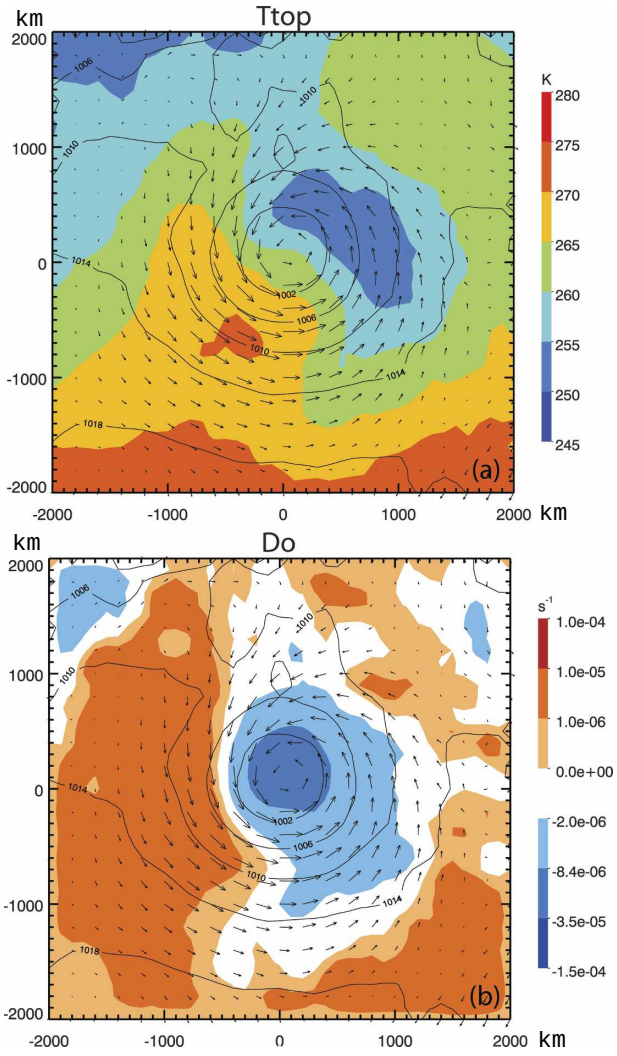

FIG. 4. As in Fig. 3 but with (a) cloud-top temperature T_{top} and (b) surface wind divergence D_0 from QuikSCAT.

by the warmest clouds ($T_{top} > 265$ K). The range of cloud top temperatures across a typical cyclone is rather underestimated in the composite field because intercyclone structural variability results in an averaging of low and high clouds together, as is clearly highlighted in the analysis of the PDFs in section 5b.

6) HORIZONTAL SURFACE WIND DIVERGENCE

The composite surface wind divergence (Fig. 4b) field shows a comma-shaped region of low-level convergence (implying large-scale ascent) to the east and south of the center of the cyclone. Low-level divergence (implying descent) is dominant at distances >1000 km from the cyclone center and is particularly strong to the west and southwest of the cyclone where there is an abundance of low clouds and few high clouds (see below). The pattern of convergence has some degree of correspondence with the rainfall pattern in Fig. 3d. This agreement suggests that it may be possible to build a moisture convergence argument to explain the observed rain rate, but the two-dimensional nature of the satellite observations would require the introduction of numerous assumptions about the three-dimensional structure of the cyclone.

7) CLOUD TYPES

High clouds are predominantly found to the east of the cyclone center (Fig. 5), with the thicker high cloud types having peak fractional coverages exceeding 27% (cirrostratus) and 12% (deep frontal) in the comma-shaped structures that are similar in size and orientation to that delineating the highest rain rates (Fig. 3d). The western edge of the cirrostratus maximum has an S-shaped appearance, which may be interpreted as the limiting streamline marking the boundaries of the warm and cold conveyor belts. The cirrus cloud extends over most of the southeast quadrant ahead of the cyclone, but high cloud is essentially absent toward the west of the system and especially where the highest surface winds are detected. Interpretation of the structure and prevalence of low-level clouds is to some extent hampered by the existence of the overlying high cloud. It is possible to make corrections using overlap assumptions, but here we present the observations without correction. Midlevel clouds are dominated by the medium thickness altostratus. This cloud type exhibits cloud fractions of >15%, especially in the northwest quadrant and flanking the northern edge of the northeast quadrant. The dominant low cloud type is cumulus that can be found over most of the domain with cloud fractions >9%, but is most prevalent in the southwest quadrant.

b. *PDF slices*

In addition to mean fields for each of the variables, our dataset can be used to examine the distribution of a variable at a given location. Here we focus upon one-dimensional slices through the North Atlantic cyclone composite and present the PDFs of variables along that locus. For all of the parameters we will consider a line ($-2000 < x < 2000$ km, $y = 0$) running across the cyclone from west to east through the cyclone center. For each point along the transect the normalized PDF of the parameter is constructed (Fig. 6).

1) CLOUD-TOP TEMPERATURE

The structure of the T_{top} PDF (Fig. 6a) is similar to a schematic cross section through a cyclone presented in

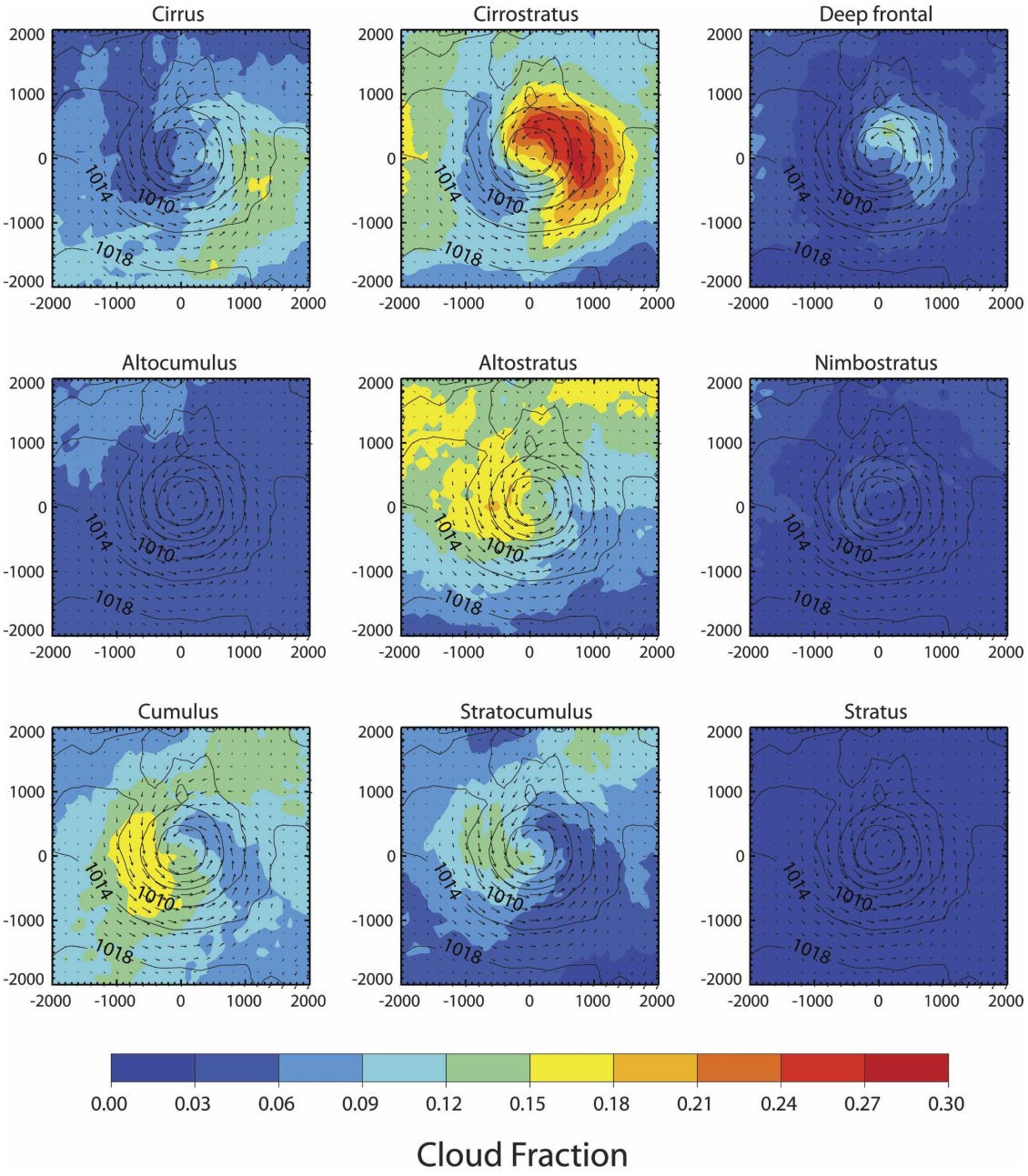

FIG. 5. Composites from the ~400 North Atlantic cyclones showing fractional coverage of different cloud types defined in section 2e: surface pressure and winds as in Fig. 3.

Carlson (1998, his Fig. 12.19b). To the west of the cyclone center the distribution of T_{top} is monomodal, does not vary strongly with location, and has a broad mode in the range 260–280 K. The warmest clouds to the west of the cyclone center are found in the region $-500 < x < -1000$ km. To the east of the cyclone center the T_{top} PDF is bimodal. The cold mode, which can be interpreted as clouds atop the warm conveyor belt, is gradually displaced to colder temperatures eastward from the center, reaching 230–240 K for $700 < x < 1200$ km, before becoming more nebulous farther eastward. The warm mode has a modal $T_{top} \sim 275$ K and extends eastward to the edge of the domain.

2) WIND SPEED

The wind speed PDF (Fig. 6b) is monomodal throughout, with peak modal values of 8–12 m s^{-1} ringing the cyclone at $x \approx -400$ km and 5–10 m s^{-1} at $x \approx$

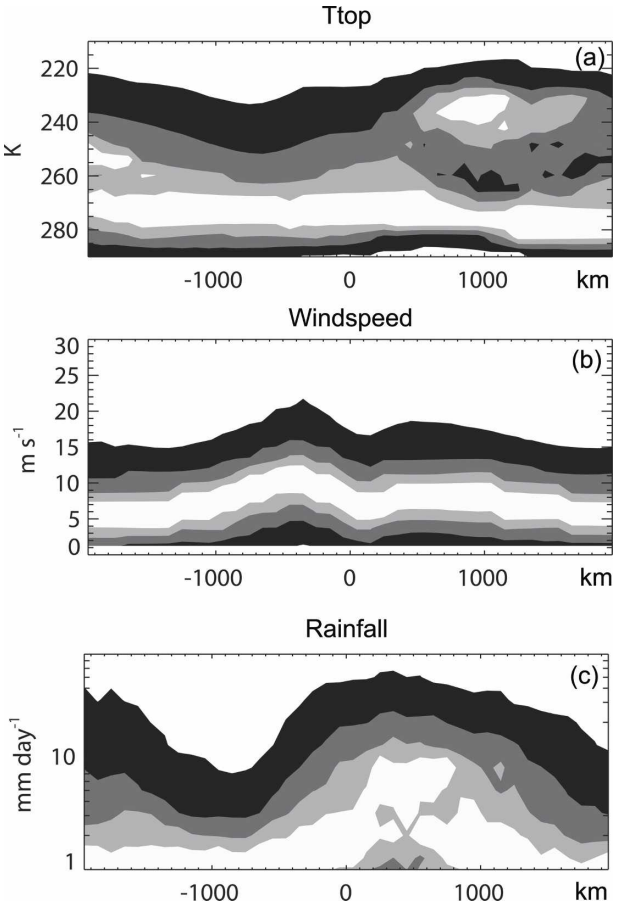

FIG. 6. Two-dimensional histograms as a function of east–west position across the center of the cyclone. The contours, from dark to light, delineate the parts of the PDF at each x position that contain 95%, 75%, 50%, and 25% of the individual cyclones. The lightest contoured region represents the mode of the PDF. (a) Cloud-top temperature T_{top}; (b) QuikSCAT surface wind speed; (c) rain rate as a function of x along $y = 0$ from the ~400 North Atlantic cyclones.

600 km, with a local minimum near the center of the system. Peak wind speed can exceed 20 m s^{-1} in the regions of strong wind a few hundred kilometers from the cyclone center.

3) RAIN RATE

The PDF of rain rate exhibits a mode that increases across the system from west to east (Fig. 6c), from ≈1–2 mm day^{-1} at $x = -500$ km to ≈2–10 mm day^{-1} at $x = 400$ km, before decreasing again to the east of the domain.

6. Regional similarity

We now examine the similarities between the composite cyclones from the four different ocean basins. Conditioning on cyclone strength $6.95 < \langle V \rangle < 8.14$ m s^{-1} and moisture $18 < \langle \text{WVP} \rangle < 21$ kg m^{-2}, to remove potential thermodynamic and dynamic bias, we show in Fig. 7 the composite mean fractional coverage of high clouds (cirrus, cirrostratus, and deep frontal combined) from the four data regions. A two-tailed t test (significant at the 99% level) is used to compare the mean high cloud fraction at each grid box from any two of the four composites constructed from between 20 and 40 cyclones. The results reveal that about 5% of the grid boxes in each of the comparisons have significantly different means. Similar results are obtained (not shown) for the other variables in this study, and for different ranges of $\langle V \rangle$ and $\langle \text{WVP} \rangle$. These results suggest that the cloud and precipitation properties of cyclones with given $\langle V \rangle$ and $\langle \text{WVP} \rangle$ are similar in all ocean basins. It may therefore be reasonably concluded that a substantial fraction of the interbasin variance in cyclone cloud and precipitation structure can be explained by systematic interbasin differences in cyclone strength and/or moisture. We further examine the dependency of cyclone clouds and precipitation upon these two metrics in the following section.

7. Clouds and precipitation as a function of $\langle V \rangle$ and $\langle \text{WVP} \rangle$

Figures 8–10 show conditional composites of rain rate, high cloud fraction, and surface wind speed, respectively, as a function both of $\langle V \rangle$ (left to right panels) and $\langle \text{WVP} \rangle$ (bottom to top panels). Mean values for parameters from each of the nine composite fields within a 2000-km radius circle can be found in Table 1. It is clear that rain rates increase with both cyclone strength and moisture (Fig. 8). It is interesting to note that the composite with the deepest low (bottom-right panel, central $p_0 < 994$ hPa) does not produce the most rain, although it is clearly associated with the greatest wind speeds (Fig. 10). In the three cyclone composites with the greatest moisture content the region of high rain rates (>5 mm day^{-1}) is located close to the cyclone center, but extends out into a comma shape to the east of the cyclone center as the cyclones intensify and eventually wrap around the low center to give a hooklike appearance in the strongest cases.

In contrast to the rain rate, high cloud fraction (Fig. 9) is only weakly dependent upon $\langle \text{WVP} \rangle$ but is strongly dependent upon $\langle V \rangle$. In all of the composites with the greatest $\langle V \rangle$ the high cloud shows a distinctive hooklike appearance as it wraps around the northwest of the cyclone center resembling the *cloud head* feature highlighted in the work of Browning and Roberts (1994). In

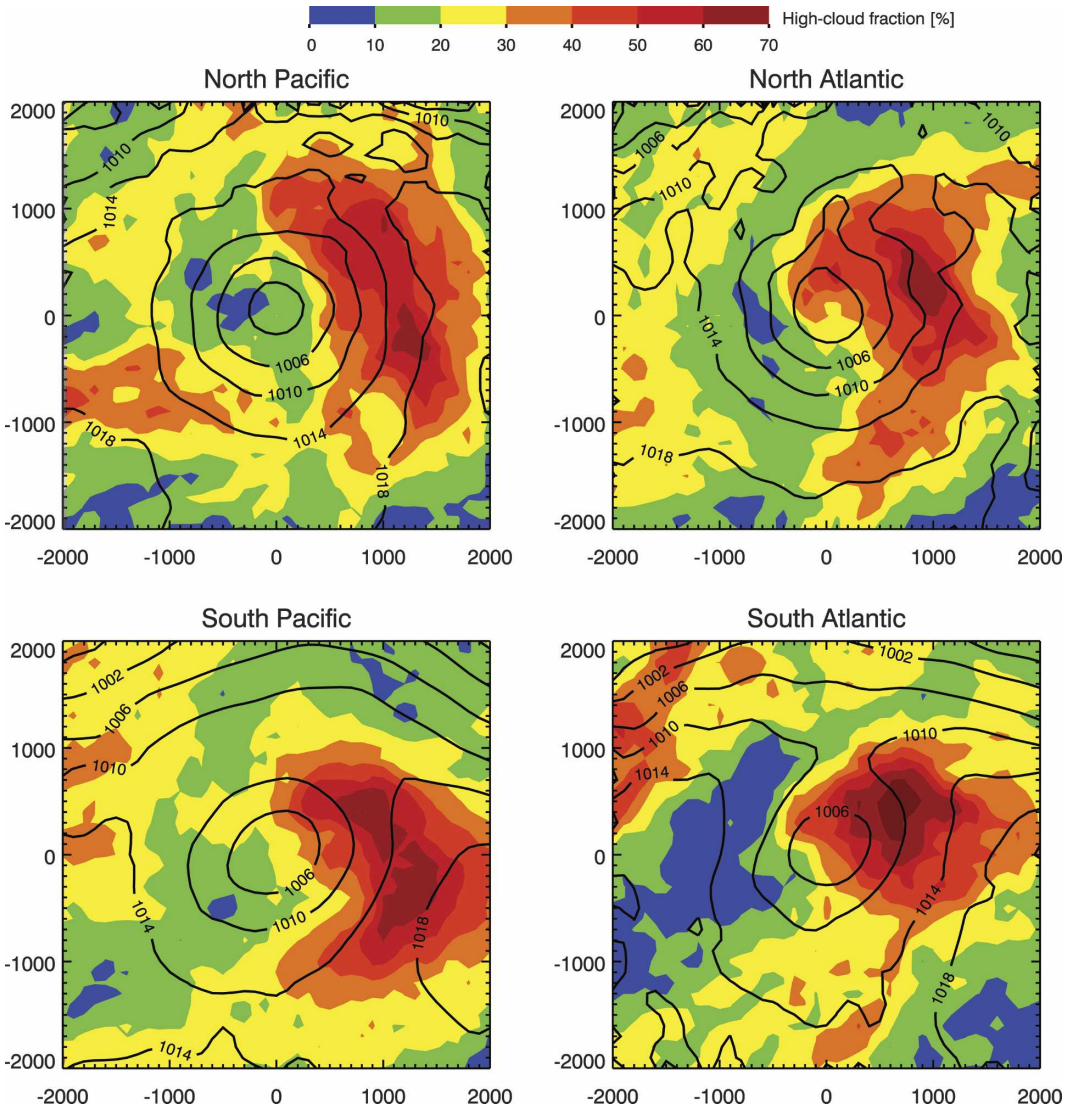

FIG. 7. High-cloud fraction composites from the North Pacific, North Atlantic, South Pacific, and South Atlantic (Southern Hemisphere data transformed into Northern Hemisphere sense) for cyclone strengths between 6.95 and 8.14 m s^{-1} and moisture between 18 and 21 kg m^{-2}.

all cases the high cloud exhibits a comma shape to the east of the cyclone center.

As expected from our definition of cyclone strength, wind speed increases with cyclone strength (Fig. 10). Of particular interest is that the position of the maximum winds moves around from west or even northwest of the cyclone center for the greatest ⟨WVP⟩ to south of the low center for the lowest ⟨WVP⟩ (Fig. 10). We speculate that because ⟨WVP⟩ is to some degree indicative of a cyclones proximity to the equator, then the location of the wind maximum may be related to the average position of the cyclone at the surface relative to the jet aloft.

To examine the composite fields in more detail we present PDFs of high cloud fraction, surface horizontal wind divergence, D_0, RH_{col}, and cloud top temperature T_{top} for the medium moisture range ($18 < \langle WVP \rangle < 21$ kg m^{-2}) and the three strength categories in Fig. 11. It can be seen that, although the means do not exhibit strong changes, the variances of the four parameters increase with $\langle V \rangle$. The D_0 PDF remains symmetrical, while the RH_{col} and high-cloud fraction PDFs become increasingly positively skewed with increasing cyclone strength. The cold cloud mode in the T_{top} PDF becomes skewed to colder temperatures as $\langle V \rangle$ increases, even forming a third, colder mode ($T_{top} = 245$ K) for the strongest storms. This confirms that the depth of the cloud systems increases with cyclone strength.

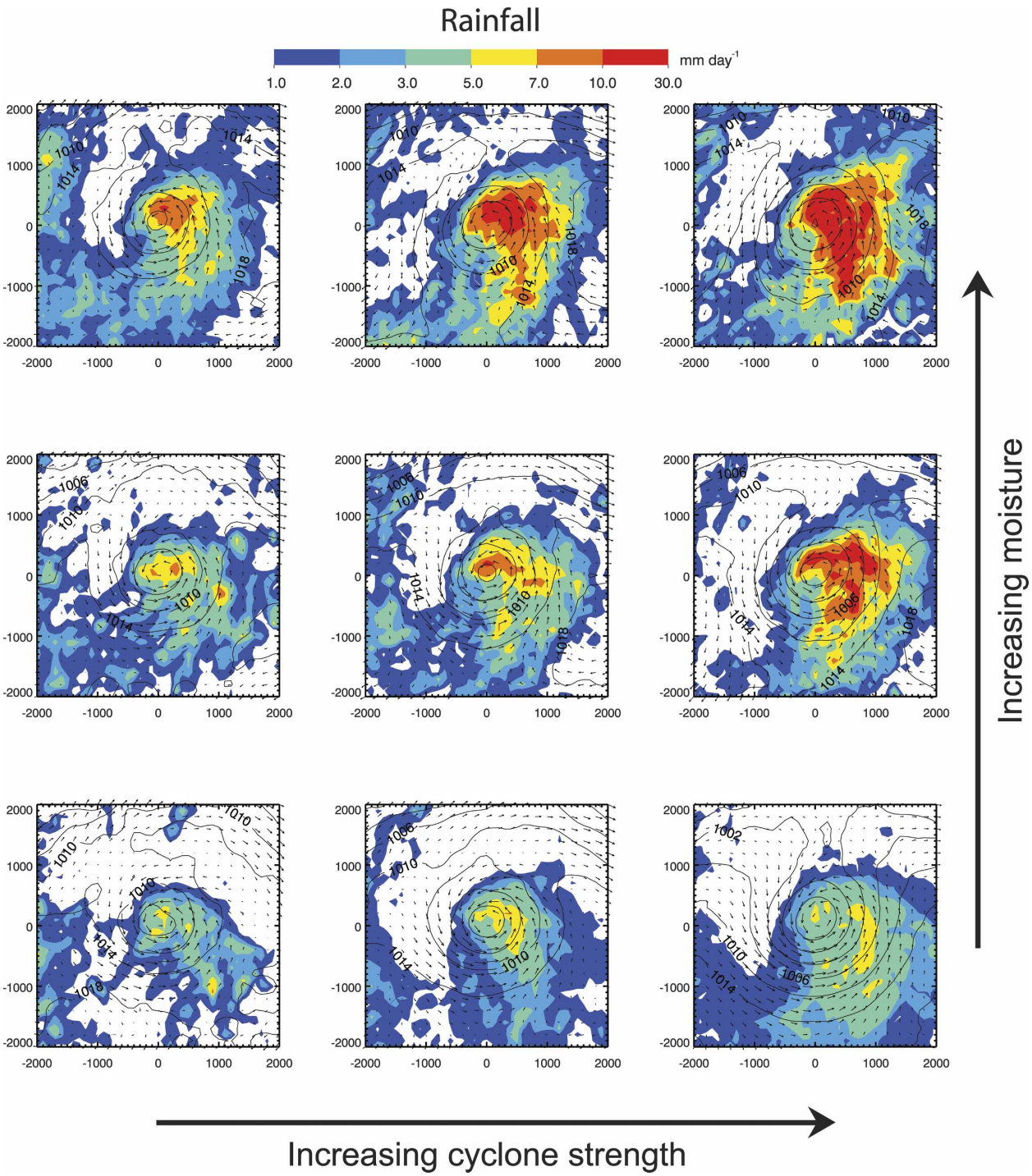

FIG. 8. Composites of rain rate for the cyclones from all four regions jointly conditioned on cyclone strength $\langle V \rangle$ (left to right) and atmospheric moisture $\langle \text{WVP} \rangle$ (bottom to top). The categories are $\langle V \rangle$: 4.9–6.95, 6.95–8.14, 8.14–12.3 m s^{-1} and $\langle \text{WVP} \rangle$: 10–18, 18–21, 21–33 kg m^{-2}. The composite mean p_0 and surface wind vectors are also shown.

Cyclonewide composite means (within 2000-km radius of the center) of a number of parameters are plotted against the mean SST (Fig. 12) and cyclone strength $\langle V \rangle$ (Fig. 13). Assuming that there are no biases in the observations, then the number of observations combined at each point in the composites will result in the random error becoming small. Therefore the error bars represent the error in the mean at 95% confidence due

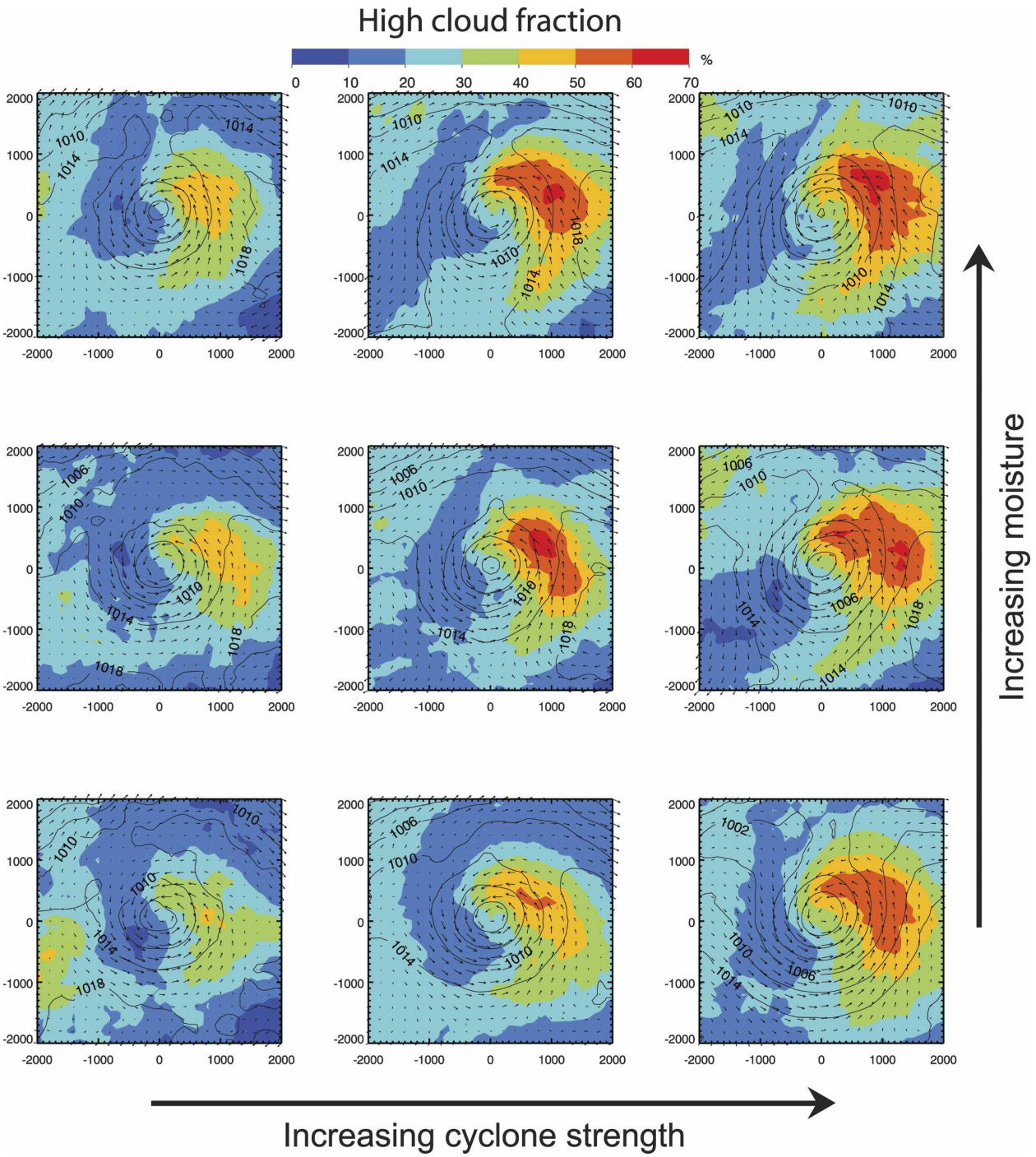

FIG. 9. As in Fig. 8 but for high-cloud fraction from MODIS.

to variability from cyclone to cyclone. These errors are obtained by calculating the weighted mean of the standard errors at each point in the composite, and then dividing by the square root of the degrees of freedom in the composite field that are determined using the spatial equivalent of the temporal autocorrelation method of Leith (1973).

The mean WVP increases with mean SST (Fig. 12a) in line with water vapor feedback arguments based upon Clausius–Clapeyron and fixed relative humidity (dashed line, e.g., Curry and Webster 1999). In contrast, the cyclone-mean RH_{col} (Fig. 12b) shows little change from 0.60 over the same 7-K increase in mean SST. Similarly, the high-cloud fraction (Fig. 12c) also shows

TABLE 1. Summary of composite mean values obtained by averaging over a circle of 2000-km radius located at the center of the domain (apart from the pressure anomaly P_a that is just the value at the center of the domain). Standard error given in parentheses.

	Dry			Medium			Moist		
	Weak	Medium	Strong	Weak	Medium	Strong	Weak	Medium	Strong
$\langle V \rangle$ (m s^{-1})	6.4 (0.2)	7.6 (0.2)	9.4 (0.2)	6.4 (0.2)	7.5 (0.2)	9.3 (0.3)	6.1 (0.1)	7.5 (0.2)	9.0 (0.3)
$\langle$WVP$\rangle$ (kg m^{-2})	15.8 (0.6)	15.4 (0.4)	14.7 (0.3)	19.5 (0.7)	19.3 (0.5)	19.3 (0.6)	25.0 (0.5)	24.7 (0.6)	23.8 (0.8)
P_a (mb)	−10.9 (0.7)	−14.4 (0.5)	−21.2 (0.5)	−13.5 (0.7)	−14.8 (0.6)	−18.7 (0.7)	−11.8 (0.3)	−14.3 (0.6)	−19.0 (0.8)
Rain rate (mm day^{-1})	1.66 (0.26)	1.93 (0.22)	2.55 (0.22)	2.17 (0.37)	2.43 (0.34)	2.82 (0.40)	2.34 (0.21)	2.73 (0.34)	3.24 (0.49)
RH_{col}	0.58 (0.01)	0.58 (0.01)	0.60 (0.01)	0.61 (0.01)	0.59 (0.01)	0.59 (0.01)	0.61 (0.01)	0.60 (0.01)	0.60 (0.01)
High-cloud fraction	0.22 (0.02)	0.26 (0.01)	0.30 (0.01)	0.23 (0.02)	0.27 (0.02)	0.30 (0.02)	0.25 (0.01)	0.29 (0.02)	0.31 (0.02)
T_{top} (K)	263.6 (1.7)	261.6 (1.1)	258.4 (0.8)	264.5 (1.6)	263.0 (1.2)	261.3 (1.4)	266.6 (0.9)	264.5 (1.0)	262.5 (1.3)
SST (K)	285.2 (0.4)	284.9 (0.3)	284.5 (0.2)	286.4 (0.4)	287.3 (0.3)	287.8 (0.3)	289.6 (0.3)	290.1 (0.3)	290.1 (0.3)
Number of cyclones	69	173	327	73	115	104	204	132	82

a tendency to remain close to a fixed value of 0.26 over the 7-K rise in mean SST, but is modulated by cyclone strength, with *greater* high cloud fraction for stronger storms.

The cyclone mean rain rate increases by approximately 50% (from about 2 to 3 mm day^{-1}) over the 7-K rise in mean SST (Fig. 12d), in line with the fractional increase in mean WVP, and close to the rise expected from arguments based upon Clausius–Clapeyron. We return to the possible consequences of this behavior in the discussion. The cyclone mean rain rate also increases markedly with cyclone strength (Fig. 13d), further confirmation that precipitation has both dynamic and thermodynamic controls.

Figure 13a shows that the mean difference in temperature between the sea surface and the cloud top increases with cyclone strength, with no clear dependency upon WVP. Thus, clouds in strong cyclones tend to extend higher into the troposphere. through the linkage between increasing cyclone strength and large-scale vertical motions.

The RH_{col} appears to remain constant with increasing cyclone strength (Fig. 13b). High cloud fraction increases from 0.23 to 0.31 with increasing cyclone strength (Fig. 13c) in spite of RH_{col} remaining constant. This suggests that moisture at low levels, which dominates the RH_{col} estimate, and high levels may be disconnected. By making a random overlap assumption we can attempt to look at changes in the medium- and low-level cloud with cyclone strength. Under this assumption, both medium- and low-level cyclone mean cloud fractions do not vary with cyclone strength exhibiting mean values of 27% (±2%) and 37% (±3%), respectively. Rain rate increases with cyclone strength (Fig. 13d), but as seen above it is just as well correlated with atmospheric moisture (Fig. 12d). This is expected from the WCB model and will be investigated in the next section.

8. Discussion

The result from the WCB model has been plotted in Fig. 14 assuming $c = 0.016$ (R_{wcb} in mm day^{-1} and $\langle$WVP$\rangle$, $\langle V \rangle$ are in SI units). The WCB model can represent with some skill the dependency of cyclonewide rain rate, and rationalizes the dependency of rain rate upon cyclone moisture $\langle$WVP$\rangle$ and strength $\langle V \rangle$. Because of the strong dependency of $\langle$WVP$\rangle$ on $\langle$SST$\rangle$ (Fig. 12a) we could equally well represent R_{wcb} as a function of $\langle V \rangle$ and $\langle$SST$\rangle$. The value for c is appropriate for means computed over a circle of radius 2000 km centered on the cyclone. It should be borne in mind that, if the radius of the circle over which the averaging

TABLE 2. Summary of seasonal composite mean values obtained by averaging over a circle of 2000-km radius located at the center of the domain (apart from the pressure anomaly P_a that is just the value at the center of the domain). Standard error given in brackets.

	Winter	Spring	Summer	Fall
$\langle V \rangle$ (m s^{-1})	9.2 (0.1)	8.0 (0.1)	6.5 (0.1)	8.3 (0.2)
$\langle WVP \rangle$ (kg m^{-2})	15.9 (0.3)	16.8 (0.3)	24.2 (0.4)	21.7 (0.4)
P_a (mb)	−19.1 (0.5)	−17.1 (0.4)	−15.0 (0.4)	−15.4 (0.5)
Rain rate (mm day^{-1})	2.56 (0.23)	2.09 (0.16)	2.55 (0.19)	2.71 (0.23)
RH_{col}	0.59 (0.01)	0.59 (0.00)	0.63 (0.01)	0.60 (0.00)
High-cloud fraction	0.31 (0.01)	0.27 (0.01)	0.23 (0.01)	0.30 (0.01)
T_{top} (K)	258.3 (0.8)	261.3 (0.6)	266.1 (0.7)	261.7 (0.8)
SST (K)	285.9 (0.2)	285.5 (0.2)	287.8 (0.2)	289.1 (0.2)
Number of cyclones	349	435	393	339

is carried out were to be increased, we would start to include rain contributions from neighboring systems. If the radius of the circle over which the averaging is carried out were reduced, we would begin to lose rain associated with the periphery of the system. Perhaps surprisingly, we find that the value of c is quite robust and only increases by ~25% if we halve the radius of the circle over which the means are computed.

The WCB model can also be used to attempt to understand seasonal variations seen in composite means of rain rate (Chang and Song 2006). In Fig. 14 we have overplotted points that represent each season (boreal winter: December–February, austral winter: June–August, etc.) from the cyclone dataset (using all ~1500 cyclones) for all regions and the mean values for cyclone strength, moisture, and rain rate are given in Table 2. It can be seen (Table 2) that variations in both cyclone strength and moisture contribute almost equally to the observed variations in rain rate. The good agreement with the WCB model leads us to suggest that the seasonal variation seen in rain-rate composites can be explained by observed variation in mean cyclone strength and moisture. The out-of-phase annual variation in the mean values of cyclone strength and moisture combine to produce the maximum mean rain rate in the fall and minimum mean rain rate in the spring.

We have assumed that there is no bias in the rain rate estimates. However, Berg et al. (2006) find that there is bias between the TRMM precipitation radar estimate of rain rate and the TRMM emittance-based retrieval that is a function of WVP. Will this adversely affect our findings? We do not think so. The ratio of rain rate between the TRMM products found by Berg et al. shows a decrease followed by an increase over the range of WVP considered here. This is markedly different from the strongly monotonic behavior we see in Fig. 14. If the TRMM precipitation radar estimates of rain rate were demonstrated to be unbiased, then we would expect that c may need to increase by 20% to accommodate the potential underestimate of midlatitude rain rate mentioned in section 2. But, the simple functional relationship linking mean cyclone-wide rain rate to ⟨WVP⟩ and $\langle V \rangle$ would remain unchanged.

To what extent can the results presented in this study be used to assess how the clouds and precipitation associated with cyclones might change as the climate warms? A complete understanding of this issue will require accurate prediction of changes in the location and strength of the midlatitude jet, which is beyond the scope of this study. However, it is possible to make some inferences as to how the cloud and precipitation in individual cyclones may change in response to changing climate. As we saw in Fig. 12, the increase in cyclone-mean rain rate with SST is close to that expected from the Clausius–Clapeyron arguments. This behavior cannot be extrapolated to estimate climatic changes in the precipitation rate of a region as a whole because these changes are more strongly constrained by the availability of energy rather than moisture (Allen and Ingram 2002). However, the observations could be useful in predicting how the precipitation rate in a particular cyclone of a given strength might increase in a warmer climate. Furthermore, if regional and global mean precipitation rates increase much more slowly than the Clausius–Clapeyron effect, as almost all global models suggest (Allen and Ingram 2002), then our results imply that either the total cyclone frequency must decrease or the mean storm strength must decrease, or both as found by Sinclair and Watterson (1999), as the mean SST rises.

Recent modeling studies suggest that the former outcome may be the more likely (Carnell and Senior 1998; Fyfe 2003). Paciorek et al. (2002) present evidence from reanalysis data suggesting that cyclone frequency in the Northern Hemisphere midlatitudes has decreased over the past half century. The overall decrease in cyclone frequency is consistent with a weaker surface meridional temperature gradient due to more rapid warming

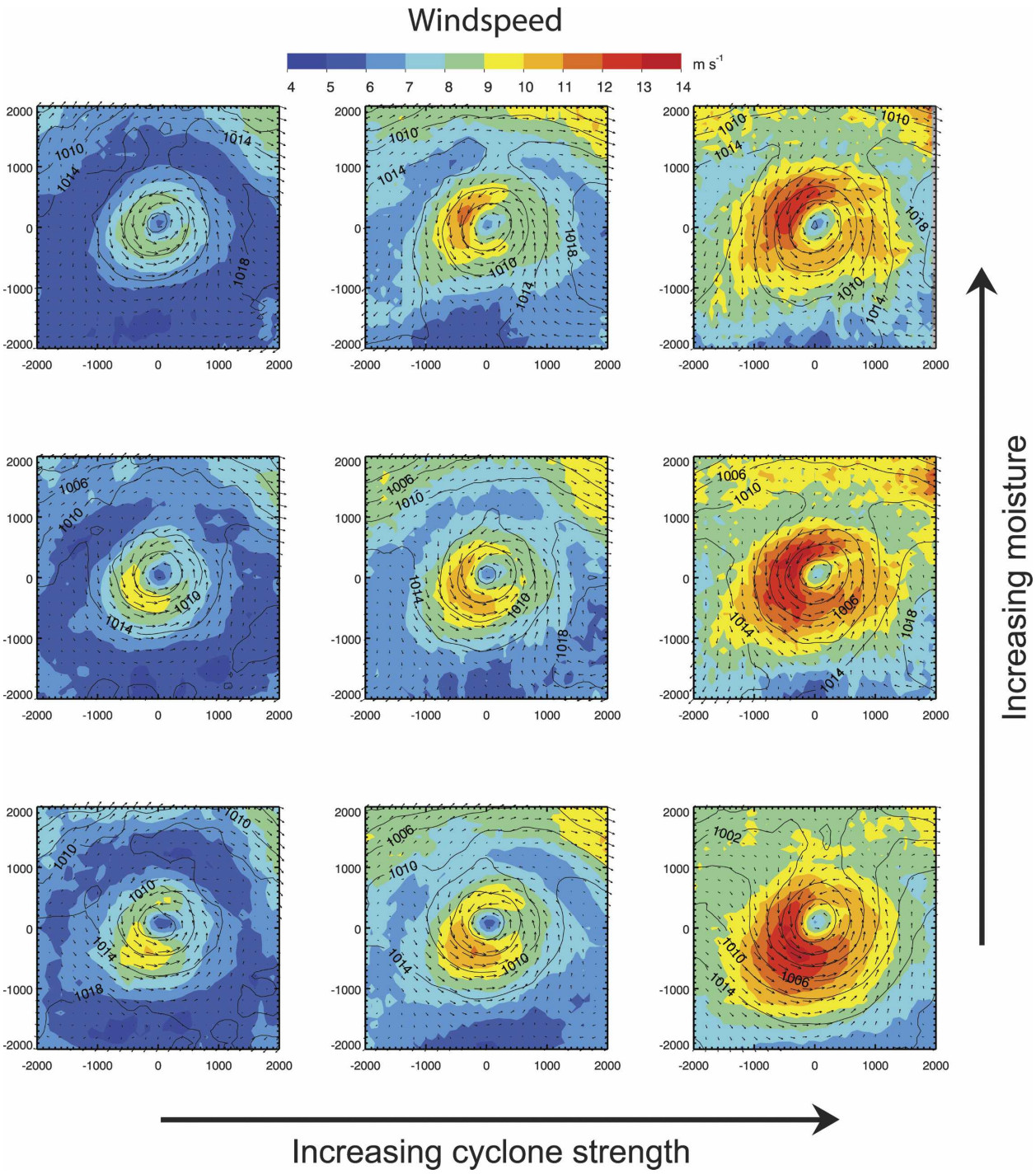

FIG. 10. As in Fig. 8 but for wind speed from QuikSCAT.

at higher latitudes caused by ice–albedo feedback. Finally, we note that, if the maximum storm strength remains close to that in the present day, then increasing SSTs could result in an increase in the probability of heavy flooding events associated with single cyclones. It would be interesting to convolve the conditional composites as a function of cyclone strength and water vapor with the interannual variability in cyclone frequency, strength, and water vapor from reanalyses and climate models, as a means for examining how the distribution and total amount of precipitation may respond to variations in climate.

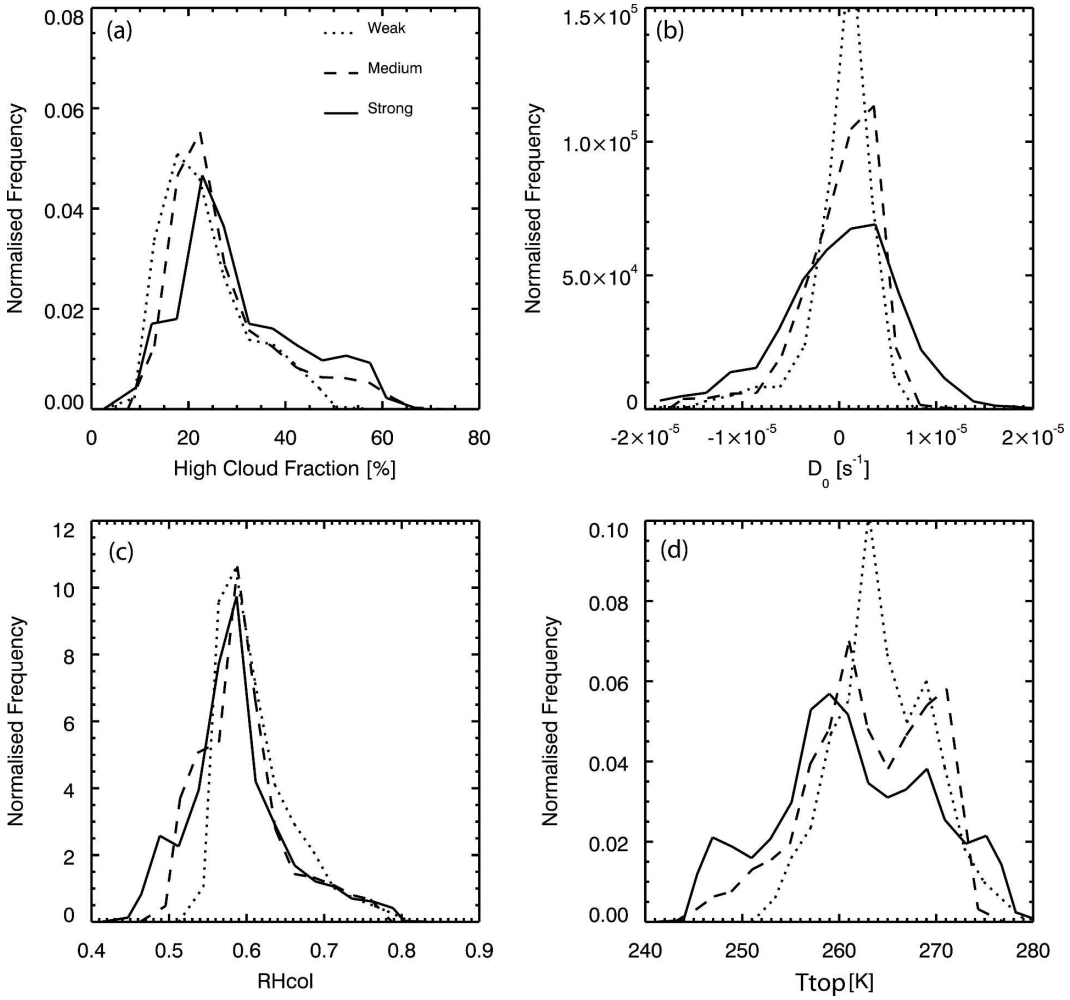

FIG. 11. Frequency distributions showing spatial variability across the $18 < \langle \mathrm{WVP} \rangle < 21$ kg m^{-2} composites of (a) high-cloud fraction, (b) horizontal surface wind divergence D_0, (c) column-relative humidity $\mathrm{RH_{col}}$, and (d) cloud-top temperature T_{top}.

Midlatitude clouds have more impact upon the earth's radiation budget than cloud systems in any other latitude belt (Harrison et al. 1990). It is clearly important to understand the possible radiative feedbacks that these changes may induce in the climate system (Stephens 2005). Some first steps in this direction have been made by Tselioudis and Rossow (2006) who present a composite observational analysis of cyclones showing an increase in the top-of-atmosphere net radiative cooling with increasing cyclone strength, and Norris and Iacobellis (2005) who conclude that increased SST leads to lower cloud amounts, while increasing the magnitude of vertical motions leads to higher cloud tops and increased optical depths. Although in this study we do not have quantitative measurements of the effect of clouds on the top of atmosphere radiation, we find in general that the high cloud amount increases significantly with cyclone strength with only a weak dependence upon water vapor path and SST. The concomitant changes in low clouds with strength and water vapor are weaker than those in the high clouds, so the increasing high clouds with cyclone strength will lead to reduced outgoing longwave radiation, and therefore net longwave warming, consistent with Norris and Iacobellis (2005) and Tselioudis and Rossow (2006). Therefore, applying the argument above, if lowered cyclone frequency and/or strength is the outcome of climate warming, then our results suggest that high cloud cover will decrease. This provides a negative feedback through increasing outgoing longwave radiation as the temperature increases.

Perhaps the most constructive use of our analysis (the data used in this analysis are available online at http://www.atmos.washington.edu/~robwood/data/

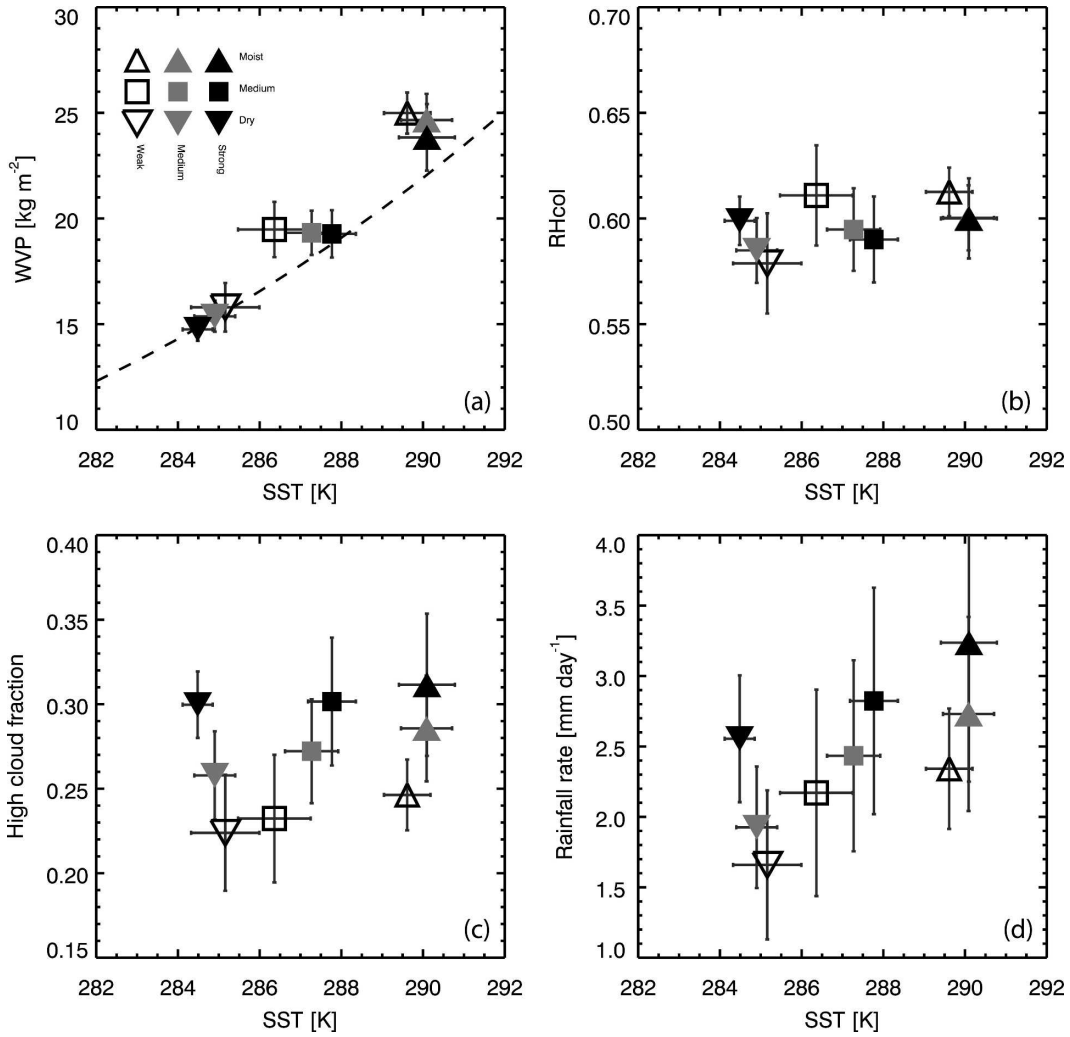

FIG. 12. Mean cyclone composite values within a 2000-km circle centered on $x = 0$, $y = 0$. Error bars represent the error in the mean at 95% confidence. These are obtained by calculating the weighted mean of the standard errors at each point in the composite, and then dividing by the square root of the degrees of freedom in the composite field that are determined using the spatial equivalent of the temporal autocorrelation method of Leith (1973). SST against (a) WVP [the dashed line represents the expected relationship from a water vapor feedback argument; see Curry and Webster (1999)]; (b) column relative humidity RH_{col}, (c) high cloud fraction, and (d) rain rate.

cyclones.html) is for the evaluation of climate models. To what extent can these models accurately represent the diagnostic relationships linking clouds, precipitation, and their thermodynamic and dynamic environment that we see in the observational data? For example, do the high clouds in climate model cyclones resemble those in the observations. Does their coverage increase markedly with the strength of the cyclones, but much less so with the water vapor path? Does the model precipitation scale with both cyclone strength and water vapor path? Answering questions such as these would constitute progress toward confidence in the model predictions of climate change.

9. Conclusions

Satellite data from the MODIS, AMSR, and QuikSCAT instruments have been used to examine the composite cloud, precipitation, and surface wind structure of midlatitude cyclones. A total of ~1500 cyclones from four midlatitude oceanic regions have been included in the analysis. The composites reveal coherent structures for all of the variables analyzed. Two metrics have been used to classify the dynamic and thermodynamic environment of the cyclones: (i) cyclone strength, based upon the areal mean surface wind speed and (ii) cyclone moisture, based upon the areal mean water vapor

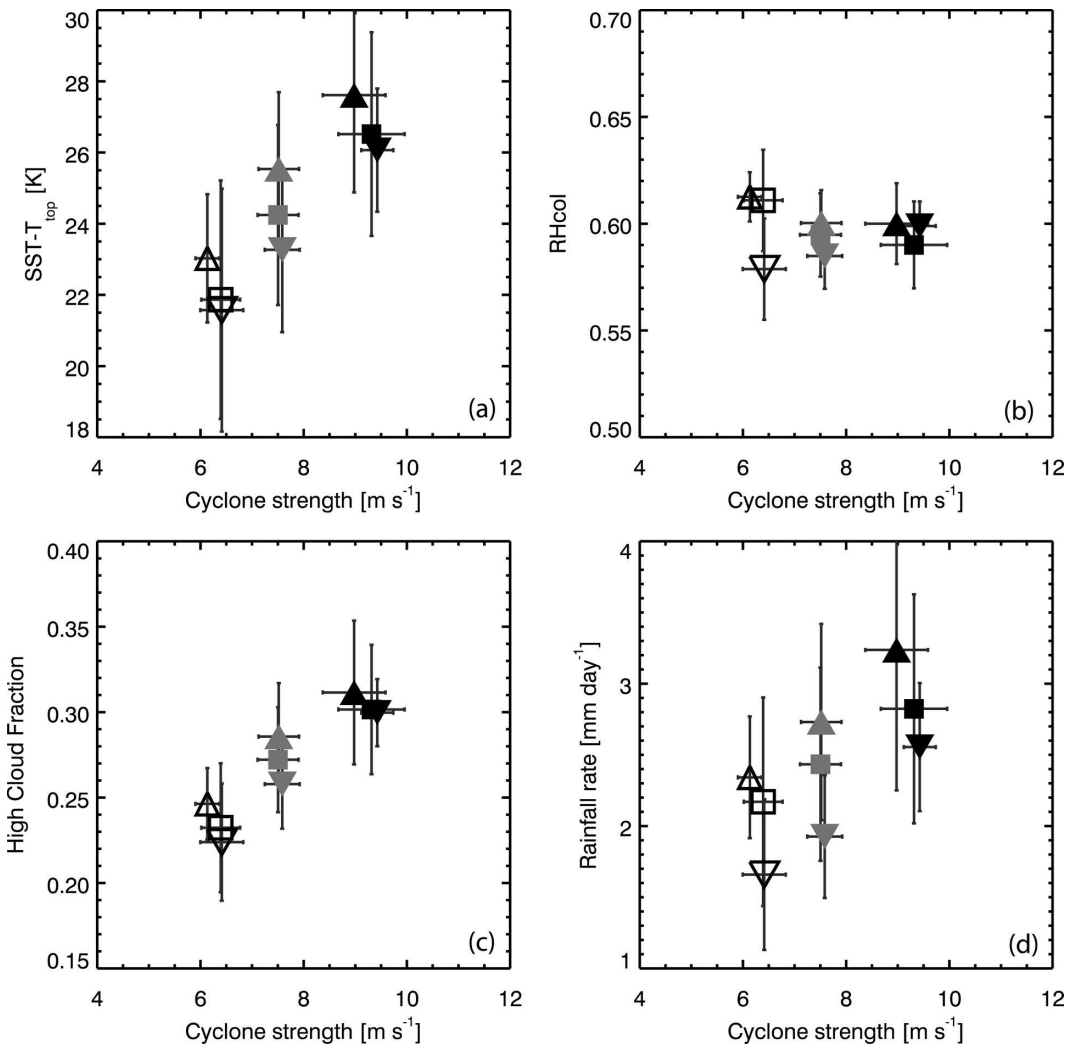

FIG. 13. As in Fig. 12 but for cyclone strength $\langle V \rangle$ against (a) T_{top} − SST difference, (b) RH_{col}, (c) high-cloud fraction, and (d) rain rate. See Fig. 12 for symbol legend.

path. The following key results were obtained by conditionally compositing cyclones according to their strength and atmospheric moisture:

- For a given strength and water vapor, cyclones are broadly similar in different geographical locations.
- Mean column relative humidity for the composite cyclones is found to remain remarkably constant (0.58–0.62) for a doubling in atmospheric moisture (equivalent to a 7-K rise in sea surface temperature) and a 50% increase in cyclone strength.
- Because vertical motions increase with cyclone strength, the rain rate and high-cloud fraction are both positively correlated with cyclone strength due to the increased flux of moisture upward in the cyclone. Rain rate is also strongly correlated with atmospheric moisture, which is in turn strongly correlated with the sea surface temperature. An increase in rain rate from 2 to 3 mm day^{-1} for a 7-K increase in sea surface temperature from 283 to 290 K is observed, roughly in line with Clausius–Clapeyron arguments. A 50% increase in the cyclone strength from 6 to 9 m s^{-1} results in an increase in high-cloud fraction from 0.22 to 0.31.
- Applying the warm conveyor belt (WCB) model to the composite cyclone observations provides a simple analytical explanation for the increase in mean rain rate with increasing atmospheric moisture and cyclone strength: increasing either variable increases the amount of moisture transported by the WCB and most of this moisture is subsequently precipitated. Simple models such as these may prove to be useful

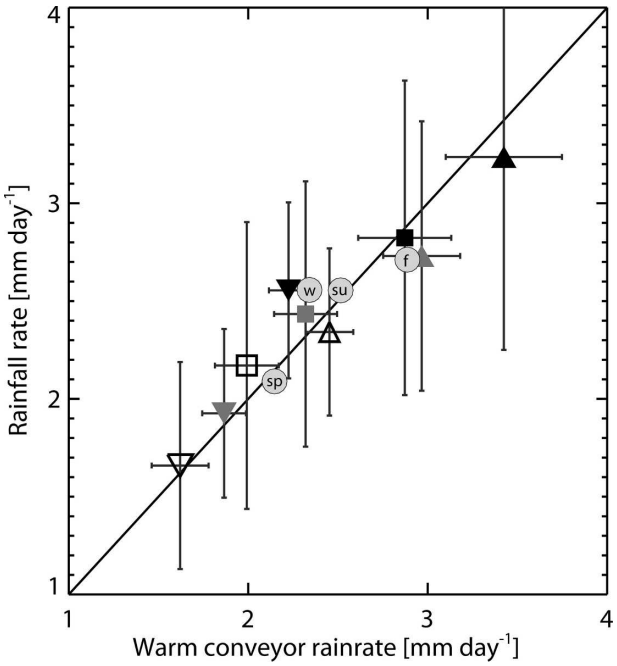

FIG. 14. Mean cyclone composite values within a 2000-km circle located at the domain center. The error bars represent twice the estimate standard error for the mean value. See Fig. 12 for symbol legend. Cyclone-mean rain rate is plotted against rain rate derived from combining cyclone strength and atmospheric moisture with a moist WCB argument. Circles represent the results from seasonal composites. w: winter [boreal December–February (DJF), austral June–August (JJA)], sp: spring [boreal March–May (MAM), austral September–November (SON)], su: summer (boreal JJA, austral DJF), f: fall (boreal SON, austral MAM).

parameterizations for minimal complexity climate models.

Acknowledgments. We thank E. Chang and one anonymous reviewer for their comments that helped improve this manuscript. We also acknowledge the NCAR (MMM) visitor program for providing funds for one of us (R. Wood) that allowed this work to be carried out. This work was supported in part by NASA Grant NNG04GA65G. AMSR-E data are produced by Remote Sensing Systems and sponsored by the NASA Earth Science REASoN DISCOVER Project and the AMSR-E Science Team. Data are available at http://www.remss.com. QuikScat data are produced by Remote Sensing Systems and sponsored by the NASA Ocean Vector Winds Science Team. Data are available at http://www.remss.com.

REFERENCES

Ackerman, S. A., K. I. Strabala, W. P. Menzel, R. A. Frey, C. C. Moeller, and L. E. Gumley, 1998: Discriminating clear sky from clouds with MODIS. *J. Geophys. Res.,* **103** (D24), 32 141–32 157.

Allen, M. R., and W. J. Ingram, 2002: Constraints on future changes in climate and the hydrological cycle. *Nature,* **419,** 224–232.

Berg, W., T. L'Ecuyer, and C. Kummerow, 2006: Rainfall climate regimes: The relationship of regional TRMM rainfall biases to the environment. *J. Appl. Meteor. Climatol.,* **45,** 434–454.

Bjerknes, J., 1919: On the structure of moving cyclones. *Mon. Wea. Rev.,* **47,** 95–99.

——, and J. Holmboe, 1944: On the theory of cyclones. *J. Meteor.,* **1,** 1–22.

Bretherton, C. S., M. E. Peters, and L. E. Back, 2004: Relationships between water vapor path and precipitation over the tropical oceans. *J. Climate,* **17,** 1517–1528.

Browning, K. A., 2004: The sting at the end of the tail: Damaging winds associated with extratropical cyclones. *Quart. J. Roy. Meteor. Soc.,* **130,** 375–399.

——, and N. M. Roberts, 1994: Structure of a frontal cyclone. *Quart. J. Roy. Meteor. Soc.,* **120,** 1535–1557.

——, and ——, 1996: Variation of frontal and precipitation structure along a cold front. *Quart. J. Roy. Meteor. Soc.,* **122,** 1845–1872.

Carlson, T. N., 1998: *Mid-Latitude Weather Systems*. Amer. Meteor. Soc., 507 pp.

Carnell, R. E., and C. A. Senior, 1998: Changes in mid latitude variability due to increasing greenhouse gases and sulphate aerosols. *Climate Dyn.,* **14,** 369–383.

Chang, E. K. M., and S. W. Song, 2006: The seasonal cycles in the distribution of precipitation around cyclones in the western North Pacific and Atlantic. *J. Atmos. Sci.,* **63,** 815–839.

Chelton, D. B., and M. H. Freilich, 2005: Scatterometer-based assessment of 10-m wind analyses from the operational ECMWF and NCEP numerical weather prediction models. *Mon. Wea. Rev.,* **133,** 409–429.

Chevalier, F., P. Bauer, G. Kelly, C. Jakob, and T. McNally, 2001: Model clouds over oceans as seen from space: Comparison with HIRS/2 and MSU radiances. *J. Climate,* **14,** 4216–4229.

Contreras, R. F., W. J. Plant, W. C. Keller, K. Hayes, and J. Nystuen, 2003: Effects of rain on Ku-band backscatter from the ocean. *J. Geophys. Res.,* **108,** 3165, doi:10.1029/2001JC001255.

Curry, J. A., and P. J. Webster, 1999: *Thermodynamics of Atmospheres and Oceans*. International Geophysics Series, Vol. 65, Academic Press, 471 pp.

Eckhardt, S., A. Stohl, H. Wernli, P. James, C. Forster, and N. Spichtinger, 2004: A 15-year climatology of warm conveyor belts. *J. Climate,* **17,** 218–237.

Evans, M. S., D. Keyser, L. F. Bosart, and G. M. Lackmann, 1994: A satellite-derived classification scheme for rapid maritime cyclogenesis. *Mon. Wea. Rev.,* **122,** 1381–1416.

Fyfe, J. C., 2003: Extratropical Southern Hemisphere cyclones: Harbingers of climate change? *J. Climate,* **16,** 2802–2805.

Harrison, E. F., P. Minnis, B. R. Barkstrom, V. Ramanathan, R. D. Cess, and G. G. Gibson, 1990: Seasonal-variation of cloud radiative forcing derived from the earth radiation budget experiment. *J. Geophys. Res.,* **95,** 18 687–18 703.

Harrold, T. W., 1973: Mechanisms influencing the distribution of precipitation within baroclinic disturbances. *Quart. J. Roy. Meteor. Soc.,* **99,** 232–251.

Hartmann, D. L., 1994: *Global Physical Climatology*. International Geophysics Series, Vol. 56, Academic Press, 411 pp.

Hoskins, B. J., and K. I. Hodges, 2005: A new perspective on

Southern Hemisphere cyclone tracks. *J. Climate,* **18,** 4108–4129.

Hou, A. Y., S. Q. Zhang, A. M. da Silva, W. S. Olson, C. D. Kummerow, and J. Simpson, 2001: Improving global analysis and short-range forecast using rainfall and moisture observations derived from TRMM and SSM/I passive microwave sensors. *Bull. Amer. Meteor. Soc.,* **82,** 659–679.

Janiskova, M., J. F. Mahfouf, and J. J. Morcrette, 2002: Preliminary studies on the variational assimilation of cloud-radiation observations. *Quart. J. Roy. Meteor. Soc.,* **128,** 2713–2736.

Kalnay, E., 2003: *Atmospheric Modeling, Data Assimilation and Predictability.* Cambridge University Press, 341 pp.

King, M. D., Y. Kaufman, W. P. Menzel, and D. Tanré, 1992: Remote sensing of cloud, aerosol, and water vapor properties from the moderate resolution imaging spectroradiometer (MODIS). *IEEE Trans. Geosci. Remote Sens.,* **30,** 2–27.

——, S.-C. Tsay, S. E. Platnick, M. Wang, and K.-N. Liou, 1997: Cloud retrieval algorithms for MODIS: Optical thickness, effective particle radius, and thermodynamic phase. MODIS Algorithm Theoretical Basis Document ATBD-MOD-05, NASA, 78 pp.

——, W. P. Menzel, and Y. Kaufman, 2003: Cloud and aerosol properties, precipitable water, and profiles of temperature and water vapor from modis. *IEEE Trans. Geosci. Remote Sens.,* **41,** 442–458.

Kistler, R., and Coauthors, 2001: The NCEP–NCAR 50-Year Reanalysis: Monthly means CD-ROM and documentation. *Bull. Amer. Meteor. Soc.,* **82,** 247–267.

Klein, S. A., and C. Jakob, 1999: Validation and sensitivities of frontal clouds simulated by the ECMWF model. *Mon. Wea. Rev.,* **127,** 2514–2531.

Kummerow, C., W. Berg, J. Thomas-Stahle, and H. Masunaga, 2006: Quantifying global uncertainties in a simple microwave rainfall algorithm. *J. Atmos. Oceanic Technol.,* **23,** 23–37.

Lau, N. C., and M. W. Crane, 1995: A satellite view of the synoptic-scale organization of cloud properties in midlatitude and tropical circulation systems. *Mon. Wea. Rev.,* **123,** 1984–2006.

——, and ——, 1997: Comparing satellite and surface observations of cloud patterns in synoptic scale circulation systems. *Mon. Wea. Rev.,* **125,** 3172–3189.

L'Ecuyer, T. S., and G. L. Stephens, 2002: An uncertainty model for Bayesian Monte Carlo retrieval algorithms: Application to the TRMM observing system. *Quart. J. Roy. Meteor. Soc.,* **128,** 1713–1737.

Leith, C. E., 1973: The standard error of time-average estimates of climatic means. *J. Appl. Meteor.,* **12,** 1066–1069.

Ma, X., Z. Wan, C. Moeller, W. Menzel, L. Gumley, and Y. Zhang, 2000: Retrieval of geophysical parameters from moderate resolution imaging spectroradiometer thermal infrared data: Evaluation of a two-step physical algorithm. *Appl. Opt.,* **39,** 3537–3550.

Neiman, P. J., M. A. Shapiro, and L. S. Fedor, 1993: The life cycle of an extratropical marine cyclone. Part II: Mesoscale structure and diagnostics. *Mon. Wea. Rev.,* **121,** 2177–2199.

Newton, C. W., and E. O. Holopainen, Eds., 1990: *Extratropical Cyclones: The Erik Palmen Memorial Volume*. Amer. Meteor. Soc., 262 pp.

Norris, J. R., and S. F. Iacobellis, 2005: North Pacific cloud feedbacks inferred from synoptic-scale dynamic and thermodynamic relationships. *J. Climate,* **18,** 4862–4878.

Oort, A. H., 1971: The observed annual cycle in the meridional transport of atmospheric energy. *J. Atmos. Sci.,* **28,** 325–339.

Paciorek, C. J., J. S. Risbey, V. Ventura, and R. D. Rosen, 2002: Multiple indices of Northern Hemisphere cyclone activity, winters 1949–99. *J. Climate,* **15,** 1573–1590.

Petterssen, S., D. L. Bradbury, and K. Pedersen, 1962: The Norwegian cyclone models in relation to heat and cold sources. *Geophys. Publ.,* **24,** 243–280.

Pincus, R., M. Szczodrak, J. Gu, and P. Austin, 1995: Uncertainty in cloud optical depth estimates made from satellite radiance measurements. *J. Climate,* **8,** 1453–1462.

Rossow, W. B., and R. A. Schiffer, 1991: ISCCP cloud data products. *Bull. Amer. Meteor. Soc.,* **72,** 2–20.

Shapiro, M. A., and S. Grønas, 1999: *The Life Cycle of Extratropical Cyclones*. Amer. Meteor. Soc., 359 pp.

Sinclair, M. R., 2002: Extratropical transition of Southwest Pacific tropical cyclones. Part I: Climatology and mean structure changes. *Mon. Wea. Rev.,* **130,** 590–609.

——, and I. G. Watterson, 1999: Objective assessment of extratropical weather systems in simulated climates. *J. Climate,* **12,** 3467–3485.

Stephens, G. L., 2005: Cloud feedbacks in the climate system: A critical review. *J. Climate,* **18,** 237–273.

Stoelinga, M. T., and Coauthors, 2003: Improvement of microphysical parameterization through observational verification experiment. *Bull. Amer. Meteor. Soc.,* **84,** 1807–1826.

Trenberth, K. E., and D. P. Stepaniak, 2003: Seamless poleward atmospheric energy transports and implications for the Hadley circulation. *J. Climate,* **16,** 3705–3721.

Tselioudis, G., and W. B. Rossow, 2006: Climate feedback implied by observed radiation and precipitation changes with midlatitude storm strength and frequency. *Geophys. Res. Lett.,* **33,** L02704, doi:10.1029/2005GL024513.

——, Y. C. Zhang, and W. B. Rossow, 2000: Cloud and radiation variations associated with northern midlatitude low and high sea level pressure regimes. *J. Climate,* **13,** 312–327.

Wang, C.-C., and J. C. Rogers, 2001: A composite study of explosive cyclogenesis in different sectors of the North Atlantic. Part I: Cyclone structure and evolution. *Mon. Wea. Rev.,* **129,** 1481–1499.

Wentz, F. J., 1997: A well calibrated ocean algorithm for special sensor microwave/imager. *J. Geophys. Res.,* **102,** 8703–8718.

——, and R. W. Spencer, 1998: SSM/I rain retrievals within a unified all-weather ocean algorithm. *J. Atmos. Sci.,* **55,** 1613–1627.

——, and D. K. Smith, 1999: A model function for the ocean normalized radar cross section at 14 GHz derived from NSCAT observations. *J. Geophys. Res.,* **104,** 11 499–11 514.

——, and T. Meissner, 2000: AMSR Ocean Algorithm. Algorithm Theoretical Basis Document Tech. Rep. version 2, Remote Sensing Systems, Santa Rosa, CA, 59 pp.

CORRIGENDUM

PAUL R. FIELD

NCAR, Boulder, Colorado

ROBERT WOOD

University of Washington, Seattle, Washington

We have discovered an error with some of the processing that affected only the rainfall rates given in Field and Wood (2007). However, the main finding from the satellite data of the success of the warm conveyor belt model to explain the rainfall rates remains unchanged upon correcting this error.

In the satellite analysis the $1^\circ \times 1^\circ$ aggregated data were screened to remove rain rates where the sea surface temperature was colder than 278 K to avoid any potential problems caused by snow/rain ambiguity associated with a low freezing level. However, this screening also inadvertently filtered out regions where the sea surface temperature could not be retrieved, where rainfall rates exceed 48 mm day^{-1} (Wentz and Meissner 2000). Therefore, the satellite data reported were biased toward lower rainfall rates. We reanalyzed the data without this incorrect screening and found that the rainfall rates for the composites were qualitatively the same as reported by Field and Wood (2007), but increased quantitatively by ~40% on average.

Here, we repeat Tables 1 and 2 where only the rain-rate row has been modified. We also reproduce (Fig. 1) the warm conveyor belt in Fig. 14 using a constant $c = 0.023$ [originally 0.016; see Eq. (1) in Field and Wood 2007]. Newly derived color Figs. 3d and 8 (not shown) are largely similar to the originals if the original color scale values are used after being multiplied by 1.35. Corrected data files and figures have been posted online (see http://www.atmos.washington.edu/~robwood/data/cyclones.html).

REFERENCES

Field, P. R., and R. Wood, 2007: Precipitation and cloud structure in midlatitude cyclones. *J. Climate,* **20,** 233–254.

Wentz, F. J., and T. Meissner, cited 2000: Algorithm Theoretical Basis Document (ATBD), version 2: AMSR Ocean Algorithm. RSS Tech. Proposal 121599A-1. Remote Sensing Systems, Santa Rosa, CA, 66 pp. [Available online at http://www.remss.com/papers/amsr/AMSR_Ocean_Algorithm_Version_2.pdf.]

Corresponding author address: Paul R. Field, NCAR, 3450 Mitchell Lane, Boulder, CO 80301.
E-mail: prfield@ucar.edu

DOI: 10.1175/JCLI4396.1

TABLE 1. Summary of composite mean values obtained by averaging over a circle of radius 2000 km located at the center of the domain (apart from the pressure anomaly P_a that is just the value at the center of the domain). Standard error given in parentheses.

	Dry			Medium			Moist		
	Weak	Medium	Strong	Weak	Medium	Strong	Weak	Medium	Strong
$\langle V \rangle$ m s^{-1}	6.4 (0.2)	7.6 (0.2)	9.4 (0.2)	6.4 (0.2)	7.5 (0.2)	9.3 (0.3)	6.1 (0.1)	7.5 (0.2)	9.0 (0.3)
$\langle$WVP$\rangle$ kg m^{-2}	15.8 (0.6)	15.4 (0.4)	14.7 (0.3)	19.5 (0.7)	19.3 (0.5)	19.3 (0.6)	25.0 (0.5)	24.7 (0.6)	23.8 (0.8)
P_a mb	−10.9 (0.7)	−14.4 (0.5)	−21.2 (0.5)	−13.5 (0.7)	−14.8 (0.6)	−18.7 (0.7)	−11.8 (0.3)	−14.3 (0.6)	−19.0 (0.8)
Rain rate mm day^{-1}	1.99 (0.30)	2.40 (0.27)	3.14 (0.27)	2.68 (0.44)	3.29 (0.44)	4.27 (0.58)	3.19 (0.29)	4.22 (0.54)	5.38 (0.76)
RH_{col}	0.58 (0.01)	0.58 (0.01)	0.60 (0.01)	0.61 (0.01)	0.59 (0.01)	0.59 (0.01)	0.61 (0.01)	0.60 (0.01)	0.60 (0.01)
High-cloud fraction	0.22 (0.02)	0.26 (0.01)	0.30 (0.01)	0.23 (0.02)	0.27 (0.02)	0.30 (0.02)	0.25 (0.01)	0.29 (0.02)	0.31 (0.02)
T_{top} K	263.6 (1.7)	261.6 (1.1)	258.4 (0.8)	264.5 (1.6)	263.0 (1.2)	261.3 (1.4)	266.6 (0.9)	264.5 (1.0)	262.5 (1.3)
SST K	285.2 (0.4)	284.9 (0.3)	284.5 (0.2)	286.4 (0.4)	287.3 (0.3)	287.8 (0.3)	289.6 (0.3)	290.1 (0.3)	290.1 (0.3)
No. of cyclones	69	173	327	73	115	104	204	132	82

TABLE 2. Summary of seasonal composite mean values obtained by averaging over a circle of radius 2000 km located at the center of the domain (apart from the pressure anomaly P_a that is just the value at the center of the domain). Standard error given in parentheses.

	Winter	Spring	Summer	Fall
$\langle V \rangle$ m s^{-1}	9.2 (0.1)	8.0 (0.1)	6.5 (0.1)	8.3 (0.2)
$\langle$WVP$\rangle$ kg m^{-2}	15.9 (0.3)	16.8 (0.3)	24.2 (0.4)	21.7 (0.4)
Pa mb	−19.1 (0.5)	−17.1 (0.4)	−15.0 (0.4)	−15.4 (0.5)
Rain rate mm day^{-1}	3.39 (0.29)	2.81 (0.22)	3.44 (0.24)	3.79 (0.31)
RHcol	0.59 (0.01)	0.59 (0.00)	0.63 (0.01)	0.60 (0.00)
High-cloud fraction	0.31 (0.01)	0.27 (0.01)	0.23 (0.01)	0.30 (0.01)
Ttop K	258.3 (0.8)	261.3 (0.6)	266.1 (0.7)	261.7 (0.8)
SST K	285.9 (0.2)	285.5 (0.2)	287.8 (0.2)	289.1 (0.2)
No. of cyclones	349	435	393	339

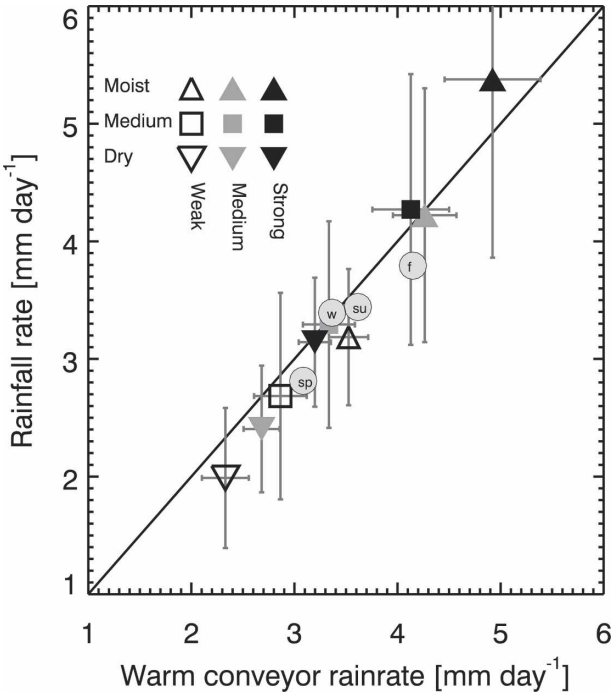

FIG. 1. New version of Fig. 14 in Field and Wood (2007). Mean cyclone composite values within a 2000-km circle located at the domain center. The error bars represent twice the estimate standard error for the mean value. Warm conveyor rain rate is plotted against rain rate derived from combining cyclone strength and atmospheric moisture with a moist warm conveyor belt argument (cyclone mean rain rate = $0.023\langle V \rangle \langle$WVP$\rangle$). The circles represent the results from seasonal composites: w: winter [boreal: December–February (DJF); austral: June–August (JJA)], sp: spring [boreal: March–May (MAM); austral: September–November (SON)], su: summer (boreal: JJA; austral: DJF), and f: fall (boreal: SON; austral: MAM).

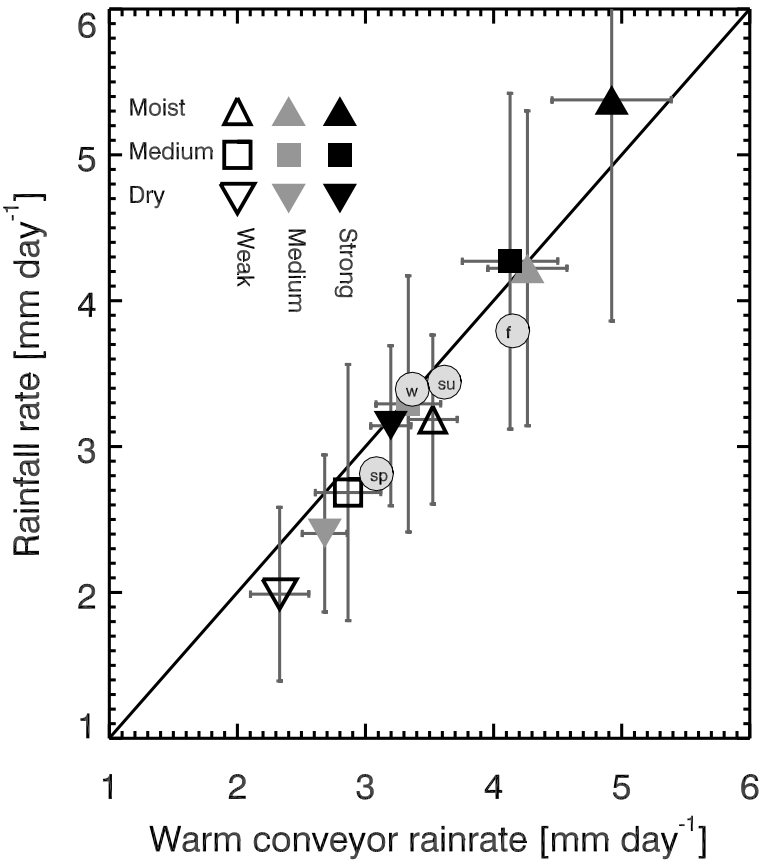

Figure 1: Mean cyclone composite values within a 2000 km circle located at the domain center. The errorbars represent twice the estimate standard error for the mean value. Cyclone mean rain rate is plotted against rain rate derived from combining cyclone strength and atmospheric moisture with a moist warm conveyor belt argument (cyclone mean rain rate = $0.023\langle V\rangle\,\langle WVP\rangle$. The circles represent the results from seasonal composites: w: winter [boreal Dec-Feb (DJF), austral Jun-Aug (JJA), sp: spring [boreal Mar-May (MAM), austral Sep-Nov (SON)], su:summer [boreal JJA, austral DJF], f: fall [boreal SON, austral MAM].

Figure 3d

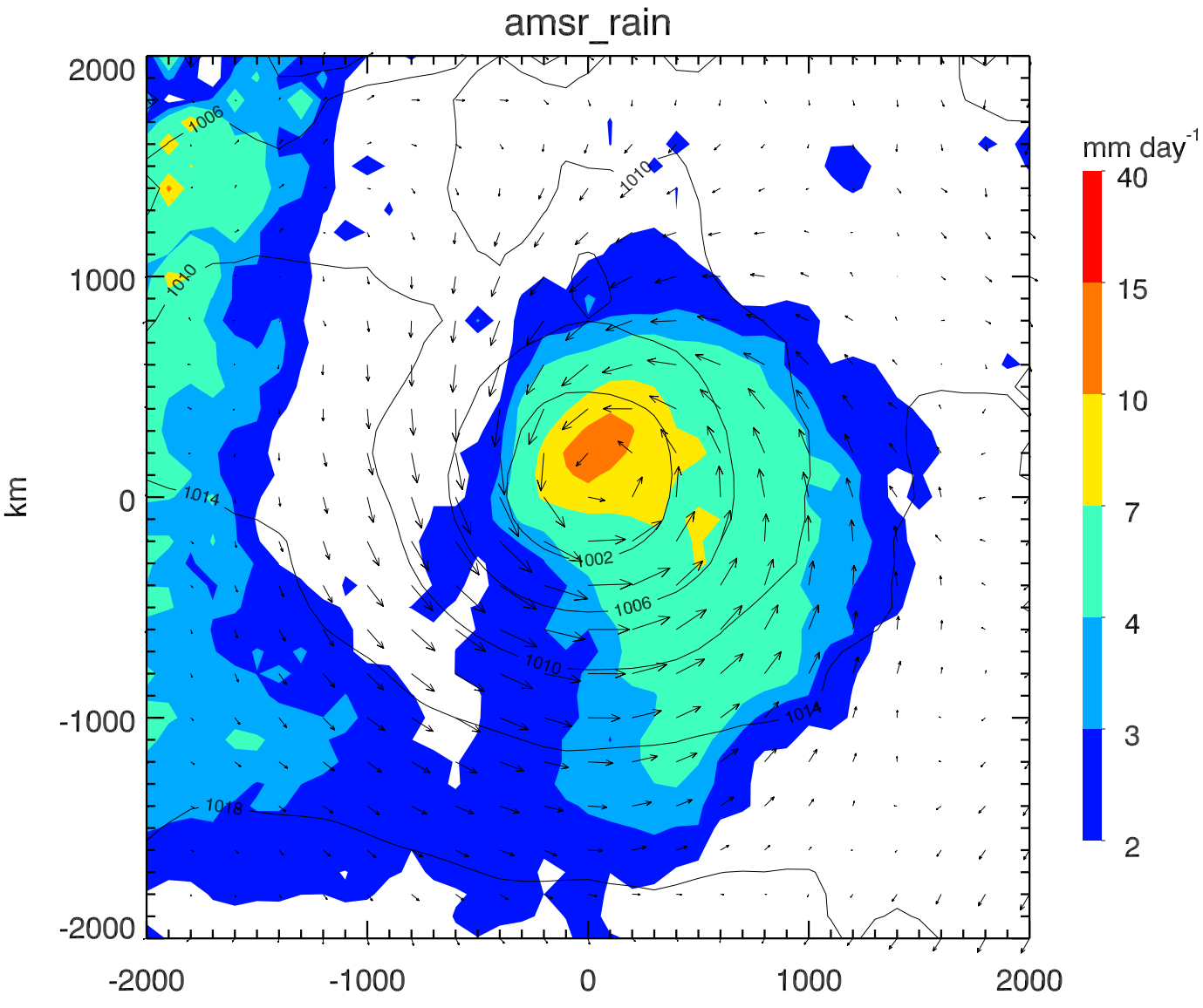
amsr_rain
2000
1000
0
-1000
-2000
km
-2000
-1000
0
1000
2000
1006
1010
1014
1002
1006
1010
1014
1018
mm day-1
40
15
10
7
4
3
2

Figure 8

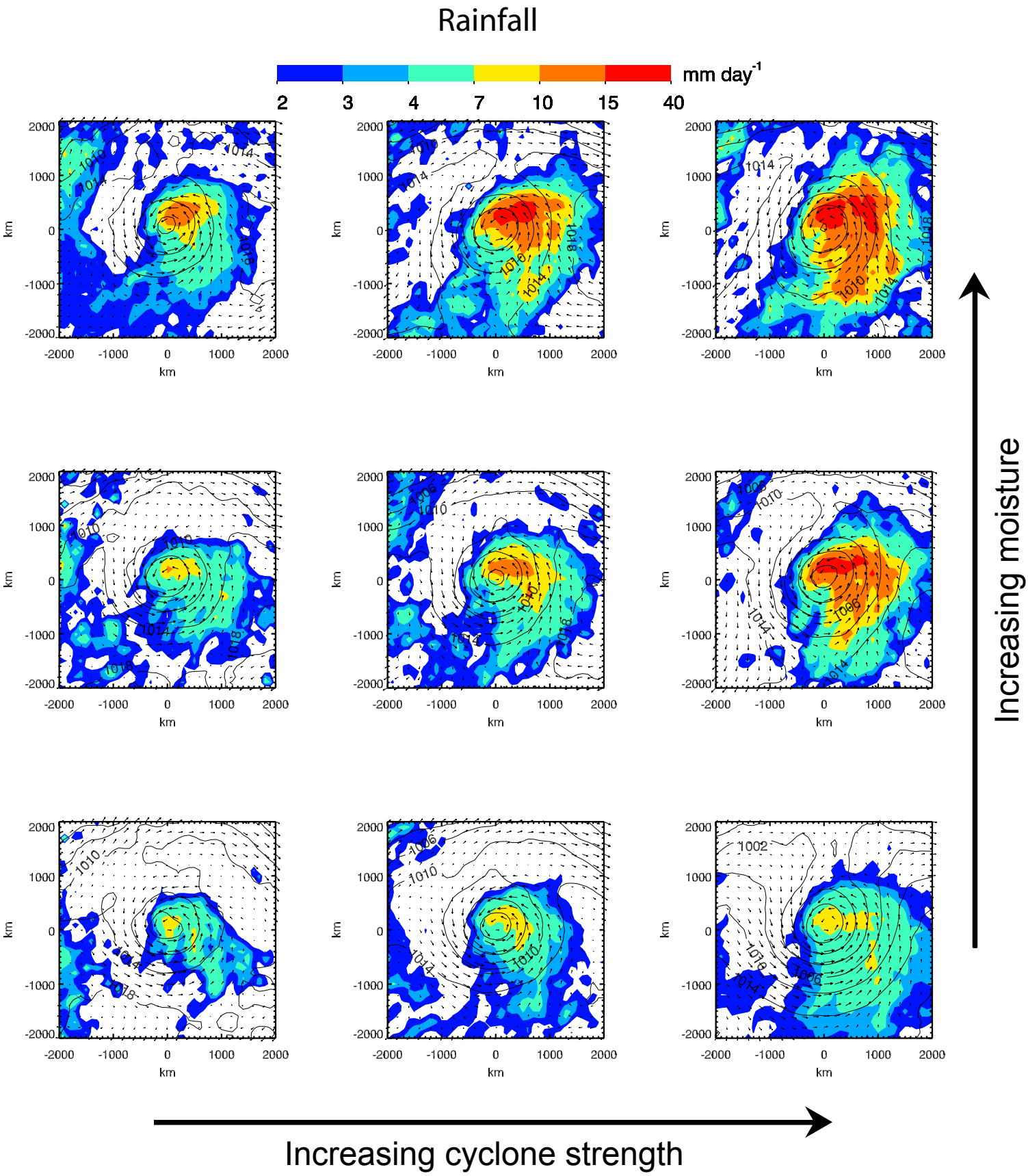
Rainfall
mm day-1
2
3
4
7
10
15
40
km
Increasing moisture
Increasing cyclone strength

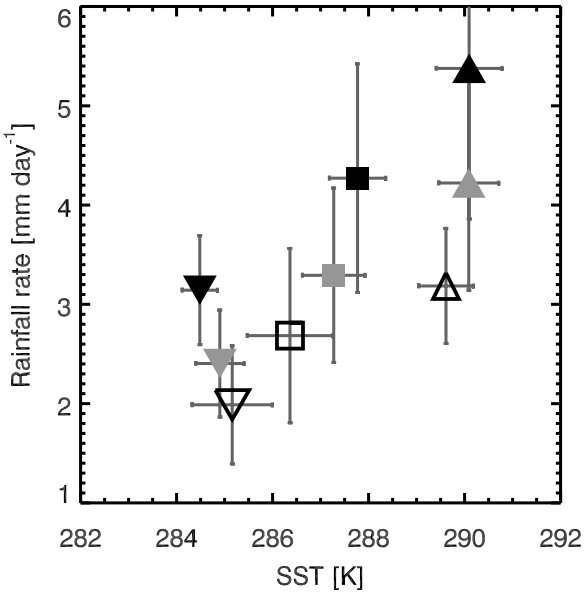

Figure 12d

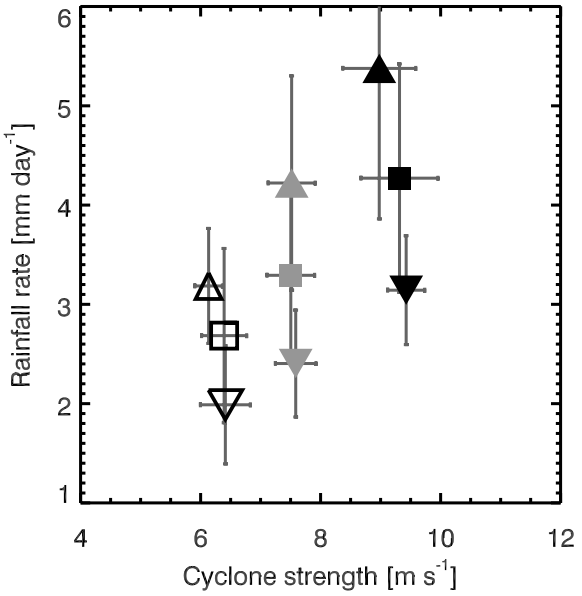

Figure 13d

Figure 14

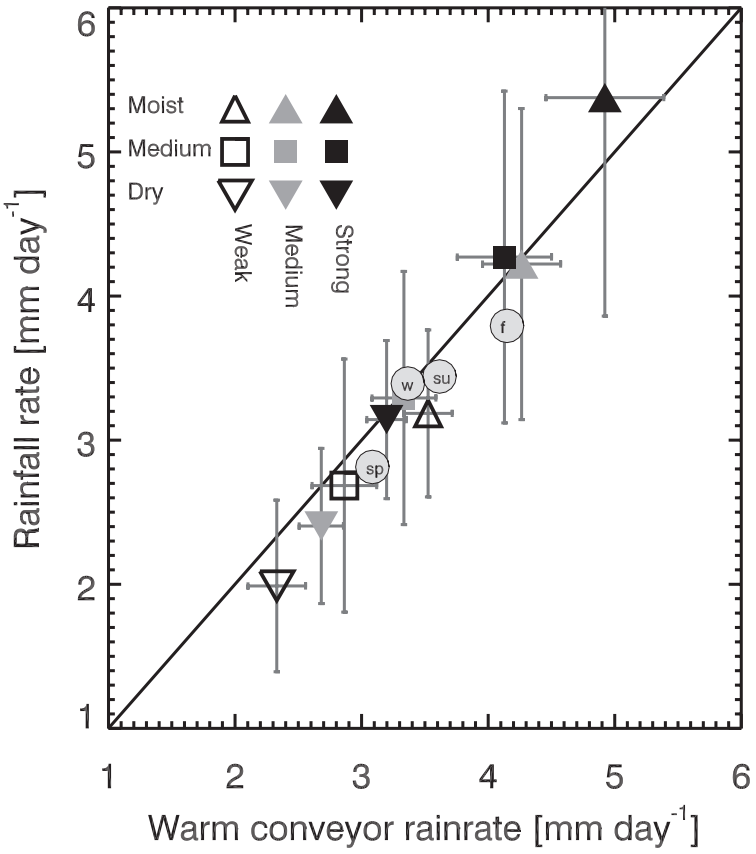
Moist
Medium
Dry
Weak
Medium
Strong
sp
su
w
f
Rainfall rate [mm day-1]
Warm conveyor rainrate [mm day-1]
1
2
3
4
5
6